Title
Electronic and Spintronic Properties of Graphene

Permalink
https://escholarship.org/uc/item/6xf233bh

Author
Pi, Keyu

Publication Date
2010

Peer reviewed|Thesis/dissertation

UNIVERSITY OF CALIFORNIA
RIVERSIDE

Electronic and Spintronic Properties of Graphene

A Dissertation submitted in partial satisfaction
of the requirements for the degree of

Doctor of Philosophy

in

Physics

by

Ke-yu Pi

August 2010

Dissertation Committee:
    Dr. Roland Kawakami, Chairperson
    Dr. Jing Shi
    Dr. Shan-Wen Tsai

The Dissertation of Ke-yu Pi is approved:

_____

_____

_____

Committee Chairperson

University of California, Riverside

Acknowledgement

I want to express my gratitude to my advisor: Professor Roland Kawakami and also my lovely lab mates. For the last six years, I have been really lucky to work closely with Roland, being one of his early students who joined the group at its building stage. With Roland's help, I have had a chance to develop myself as an independent researcher and learned how to systematically approach an open-ended question. For me, he is more than just an advisor, but a mentor. I also want to acknowledge the impact of my lab mates: Wei Han and Kathleen McCreary worked with me and have contributed a lot to the projects in this thesis; Richard Chiang, Yan Li, Jared Wong, Adrian Swartz and Desalegne Teweldebrhan were always available to discuss the projects with me and have offered many good ideas; Former postdoctoral researchers Wei-Hua Wang, Ramesh Thamankar, and Yewhee Chye taught me a lot of lab techniques. Because of them, I enjoyed working in the lab.   Although all my family is in Taiwan, these lovely lab mates make me feel at home.

I was born in a traditional Taiwanese family. Just like other Taiwanese parents, they are not used to showing their emotions. Even so, I can still clearly remember the day I decided to do my graduate school in the United States and they were standing outside the security check point at the airport. I can see the sadness on my parents' and grand parents' faces, but they hold back their tears to be supportive. It felt like they lost something valuable and might not get it back.

I love you grandpa, grandma, dad, mom and brother. Thank you for always being there for me. Because you love me, I can always stay happy, stay passionate and stay optimistic.

I want to acknowledge my collaborators; Prof. Jeanie Lau, Prof. Jing Shi, and Prof. Shan-Wen Tsai and their group members. They were really helpful both on experimental techniques development and theoretical analysis. I also received help from our machine shop staff; Mike, Daniel, and Dave as well as our cleanroom staff; Dong and Dexter. With their help, I was able to get the experiment working without being sidetracked and wasting time.

There are a lots of good friends that keep me company in Riverside: Eric Chang, Kevin Kao, Eric Chien, Hank Huang, Sean Wang, Chris Tsai, Pearl Chen, Gang Liu, Feng Miao, Xin Zhang, Miaogeng Zhang, Xiaowei Yu, Li Zeng, Li Zhang and many others friends I met in United States. Thank you for sharing exciting things, exploring new areas and tasting delicious foods with me. You guys will be an important piece of my memories that I will never forget. At the end, I want to say thank you to my girl friend, Min Yang, who is a pleasant surprise that happened in my life. By sharing everything with her, all the happiness in my life was double and all sadness reduced by half. I was really lucky to meet her.

致謝

我很幸運的能夠跟一個關心我, 照顧我的指導教授 Roland Kawakami, 還有一群可愛的實驗夥伴, 一起度過過去六年的日子. 能夠在實驗室草創之初, 加入這個實驗, 跟充滿研究熱誠的Roland 一起工作, 是千金難換的經驗. 在這裡, 我學會獨立研究的方法, 也體驗到向未知的問題挑戰的過程. 對我來說, Roland 不僅僅是個指導教授, 更是個亦師亦友的心靈導師. 我也想要感謝跟我一起挑燈夜戰, 一起得到很多實驗成果的 韓偉跟Kathleen McCreary. 跟我分享很多實驗想法, 跟我討論的 李妍,江岳峰, Jared Wong, Adrian Swartz 和 Desalegne Teweldebrhan. 還有指導我很多實驗技巧的 三個博士後研究員: 王偉華, Ramesh Thamankar 跟 Yewhee Chye. 因為有這些人的存在, 實驗室對背井離鄉的我來說, 更像是家. 這些人,就是我在美國的家人. 實驗室變成一個有趣而安慰的存在.

我的家人是很傳統的台灣家庭. 一如其他的傳統父母, 我的父母親跟爺爺奶奶, 也是不擅於表達自己感情的人. 及使如此, 我還是很清楚的記得, 我決定出國念書, 在機場轉身離開時他們臉上的不捨跟淚水. 對於他們, 我心中充滿了內疚和感恩. 為了完成自己的理想, 不能留在台灣陪著他們. 也謝謝他們能理解我, 不論如何, 都給我支持. 謝謝妳們, 我愛妳們 –皮奶奶, 皮老爸, 皮老媽, 皮克勤 跟 天上的皮爺爺. 也謝謝我所有其他的家人. 因為妳們愛我, 所以我總是可以堅強的面對困難而且保持樂觀.

在實驗的過程中, 我跟Prof. Jeanie Lau, Prof. Jing Shi 和 Prof. Shan-Wen Tsai 的研究團隊在實驗和理論上有很多的合作, 獲益良多. 我也從學校的機械工廠的Mike, Daniel 和 Dave還有無塵室的Dong跟 Dexter那邊得到了很多的幫助. 因為有他們, 我的實驗才能夠順利的進行, 他們幫助我少走了很多的冤枉路.

也很感謝我身邊的很多朋友, 他們是我在美國的重要回憶. 因為有他們, 我再實驗室以外的生活不會孤單. 跟他們一起探索美國的文化, 品嘗美國的美食, 參觀旅行美國的自然景觀都是很難忘的事情. 謝謝妳們 :張家誠, 高世權, 黃廷楷, 簡正忠, 王奕翔, 蔡俊霖, 陳永宜, Gang Liu, Feng Miao, Xin Zhang, Miaogeng Zhang, Xiaowei Yu, Li Zeng, Li Zhang 和所有我在美國認識的朋友們. 當然還有我最重要的寶貝蛋~ 楊敏. 她總是在我身邊跟我分享我的喜怒哀樂. 她總是用她的快樂活力感染我, 然後幫我一起分擔不愉快的情緒. 謝謝妳～ 寶貝.

ABSTRACT OF THE DISSERTATION

Electronic and Spintronic Properties of Graphene

by

Ke-yu Pi

Doctor of Philosophy, Graduate Program in Physics
University of California, Riverside, August 2010
Dr. Roland Kawakami, Chairperson

  In this thesis, I summarize our studies investigating the electronic properties and spintronic properties of transition metal doped graphene over the last six years. In chapter 2, I will be talking about the device fabrication steps including our graphene exfoliation, graphene identification, ebeam lithography steps and electrode metallization. The measurement setup, including our molecular epitaxy system (MBE) and AC lock-in measurement, will also be discussed in detail.

  To utilize graphene as an electronic base material, it is important to understand the interface between contact electrodes and graphene. Transition metals (TMs) have been widely used as a contact material for graphene devices but the charge transfer mechanism between TMs and graphene was not well understood. A specially designed MBE system was built to deposit TM atoms onto graphene devices and to measure the magnetotransport properties *in situ*. In chapter 3, I will be discussing our experimental studies on the charge transfer, scattering, and effects of cluster formation on graphene. These results are important for improving the performance of graphene electronic devices.

For graphene spintronics, one of the most important questions is the spin relaxation mechanism in graphene. It is theoretically predicted to have a long spin lifetime of over 1 ms. However, spin lifetimes observed are only about 200 ps. The big difference between these two values is an important scientific question to address in order to achieve long spin diffusion length. In chapter 4, I utilized molecular beam epitaxial growth to systematically study the spin lifetime in graphene. It is demonstrated that Coulomb scattering (charged impurities) is not the dominant spin relaxation mechanism.

Table of Contents

List of figures

Chapter 1: Introduction

CMOS based electronic devices have been following Moore's law[1] for the past twenty years, but their progress is expected to run out the steam soon. The search for a material to replace silicon has been an important issue in both industry and academics. At the same time, rapid development of an area known as spintronics is looking at utilizes the quantum mechanic properties of the electron, the spin degree of freedom, has brought a big impact in the information process and memory storage devices[2-5]. The discovery of giant magnetoresistance (GMR) [2] [28] and tunneling magnetoresistance (TMR)[3-5] effects has led to the application of spintronics in data storage devices and magnetoresistive random access memory (MRAM) devices. Many researches are trying to demonstrate the potential of using spintronic devices as logic devices. Professor Lu Sham from UCSD proposed the idea of using spin transport devices as the logic gate devices[29, 30]. For future applications and research interest, it will be ideal if we can integrate the electronic devices and spintronic devices. To achieve this goal, we need to have a base material that has great properties for both electronics and spintronics.

Graphene, a single layer of carbon atoms, was discovered in 2004 and soon became an attractive material for exploring novel physics[6-8]. Many believed graphene could not exist in nature until Andre Geim's group[6, 9] successfully demonstrated that graphene could exist by micro mechanical exfoliation of graphene from HOPG on a Si/SiO_2 substrate. Graphene demonstrated amazing electronic properties, including high mobility[10-12] and tunable carrier type. By applying a gate voltage to the device, we can

either attract electrons with positive gate voltage or repeal electrons and create hole transport with negative gate voltage. The signature gate dependent conductivity curve shows a clear conductance minimum at the Dirac point. In such a perfectly defined two-dimensional system, many 2D physics phenomena have also been investigated such as quantum Hall effect[6, 8, 13] and fractional quantum Hall effect[14-16]. Due to its unique linear dispersion band structure, electrons and holes are expected to behave as massless dirac fermions in this material. Additionally, the potential for high frequency electronic devices have been demonstrated up to 100 GHz in this system[17].

With this 2D electronic material, we can expose most of the conducting area to the outside world and change the transport properties by surface chemical doping. Studies consisting of doping graphene with various gases has been performed by a different research team[18]. The conductivity of graphene clearly changed with various amounts of doping and results suggested that we can utilize graphene's special properties for gas or chemical sensors[19, 20].

How these different types of doping introduce scattering mechanisms into graphene is also an important question for graphene electronic devices. Many theoretical works addresses this topic[21-23] and many experimental works are trying to identify the dominant charge scattering mechanism in graphen such as charged impurities[19], acoustic phonons[24, 25], surface corrugations[26], etc. By understanding how these factors affected the charge transport in graphene can help us improve graphene electronic

devices. With all these efforts, there is a good chance that graphene can be useful in the future technology.

Over the last few decades, spin has been optically or electrically detected in many different materials, such as metals[27, 28], semiconductors[29-31], organic molecules[32], carbon nanotubes[33, 34], and graphene[35-38], etc. Among these materials, graphene is the first gate tunable device to demonstrate lateral spin transport at room temperature [39]. Due to its low spin orbital coupling and weak hyperfine interaction, graphene is expected to have long spin lifetime and long spin diffusion length. However, the highest spin lifetime that has been measured in graphene is less than few hundreds ps which is about 1000 times smaller than the theoretical prediction[40-43]. Therefore, understanding the spin relaxation mechanisms in graphene can further improve the spin properties in graphene and bring us closer to the spin logic devices[35, 44-46].

Graphene has already shown its great characteristics for both electronics and spintronics. Recent developments of large area graphene growth make it even more attractive for future applications[47, 48]. My studies in this thesis improve the understanding of charge transfer mechanism and charge scattering mechanism by introducing transition metals (TM) in contact with graphene[49]. One important result is the experimental observation of an interfacial dipole at the TM-graphene interface, which has been predicted theoretically[50, 51] [chapter 3]. I also provide experimental evidence to rule out the charged impurities as the dominant spin relaxation mechanism in graphene,

even though they are very important for momentum scattering. Furthermore, I also find that spin lifetime can be enhanced by surface chemical doping on graphene[44].

Chapter 2: Device Fabrication and *in-situ* measurement:

2.1: Device Fabrication.

In this thesis, there are two different types of devices used, the graphene field effect transistor and the graphene spin valve device. In this section, I will talk about the general steps of fabrication for both type of devices and any detailed differences will be discussed later in the following chapters. For our devices, we exfoliate graphene from highly oriented pyrolytic graphite (HOPG) or Kish graphite. First, we apply the Scotch tape to the HOPG or Kish graphite and carefully peel off a thin layer of graphite. With the thin layer of graphite transferred onto tape, we repeatedly apply and peel the tape on this thin layer of graphite until it has smooth surface. Then the graphite is rubbed onto the SiO_2 (300 nm)/Si substrate transferring pieces of graphene and graphite onto the substrate. The SiO_2/Si allows us to easily identify graphene under optical microscope [Figure 2.1a]. The single layer graphene flakes are confirmed by the Raman spectroscopy [52], which uses laser wavelength of 532nm [Figure 2.1b]. After confirmation, the sample was loaded into to the Fisher scientific tube furnace and annealed in O_2 environment to remove any impurities on the graphene.
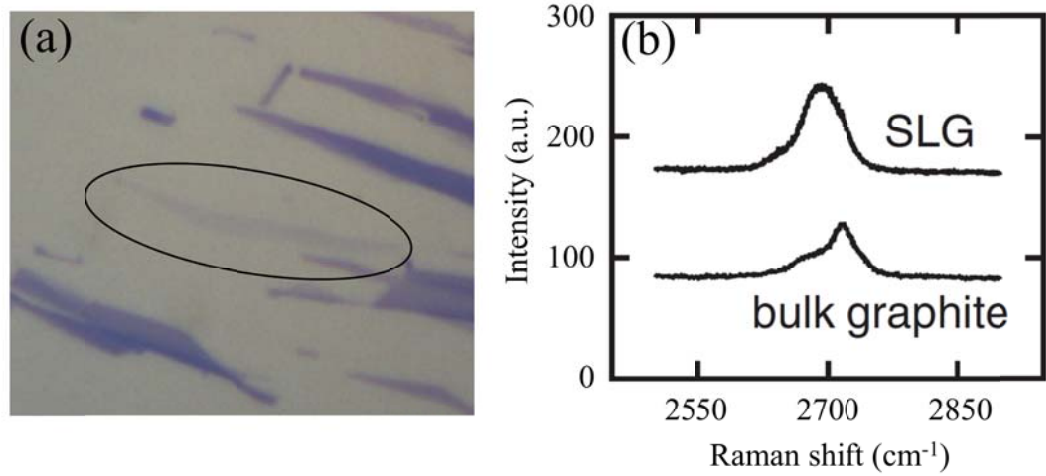
Figure 2.1 (a). Optical image of single layer graphene. (b). Comparison of Raman spectrum for single layer graphene and bulk graphite.

To make the electrodes for the graphene devices, we use ebeam lithography to define the electrode patterns. For our lithography, we use a bi-layer resist of methyl methacrylate (MMA) / Poly(methyl methacrylate) (PMMA). We first spin coat the MMA at 3200 RPM for 40 second followed by 5 minute bake at 180 ^{0}C to harden the resist. Once the sample has cooled to room temperature, we spin coat the PMMA (MicroChem 950K A4) resist at 3200 RPM for 40 second and bake at 180 ^{0}C for 20 minute on the hot plate. These steps will give us totally 500 nm of ebeam resist[53]. The reason for using MMA/PMMA bi-layer resist is because MMA is more reactive than PMMA for same amount of ebeam exposure time (Leo 1550, Aperture = 20 μm, Beam energy = 30kV). Therefore, when exposing the pattern for the electrodes, we are able to create a slight

undercut with this MMA/PMMA resist structure which helps create clean electrode edge without the roughness caused by the lift off process.

The first step before patterning the device is to locate the graphene piece that is going to be used for the device. We designed a big matrix of alignment marks composed of small crosses every 50 μm and a reference number every 500 μm [figure 2.2]. These alignment marks were put down in the area where graphene flake is located through ebeam lithography. Following by the ebeam exposure, we dip the sample into chemical solvent mix of Isopropanol (IPA) and Methyl isobutyl ketone (MIBK) (3:1, respectively) for 80 second to develop the alignment marks (areas resist that has been exposed to the electron beam will be removed).

Figure 2.2 Ebeam pattern for alignment marks. In between the crosses, there is a 50 mm spacing and we have numbers for coordinates every 500 mm.

In order to minimize the resist residues left on the graphene, we simplify our fabrication procedure by reducing the number of steps of ebeam lithography. Usually, a thin layer of Ti and Au are deposited followed by a lift-off process to metalize the alignment patterns, making it easier to see the alignment marks inside the ebeam writer. This means though, that all the steps for spin coating the resist must be repeated for pattering the electrodes. However, we developed a slightly different method. We spin-coat our MMA/PMMA bi-layer resist, use the ebeam lithography to write our alignment marks and develop the alignment marks with the IPA/MIBK mixture mentioned earlier. Once the alignment marks have been developed, the sample is loaded back into the SEM/ebeam writer. By carefully tuning the contrast and brightness, we found the resist alignment marks are still clearly visible under SEM microscope and there was no need for any metallization. This means only a single spin-coating process is needed for the whole device fabrication minimizing the resist residue left on the graphene device. With alignment marks surrounding graphene flake, we can get the relative position between alignment marks and the target graphene flake. Once everything is aligned, a second ebeam lithography step is used to pattern the contact electrodes on to the graphene with offset no more than 100 nm.

One concern for this method is the controllability of the second lithography step (the electdoes). Because the ebeam resist has been dipped into the developer and rinsed by Isopropanol (IPA), the resist layer is expected to become softer. Through careful calibration and introducing a short baking on the hot plate to dry out the IPA residue, we are able to consistently pattern well defined sharp electrodes down to 80 nm in width.

After the electrode patterns have been developed, we load the sample into the evaporation system and deposit metal everywhere on the chip. Once the desired metal has been deposited, sample was then dipped into Positive radiation (PG) remover with 70 ^{0}C for about 30 minute to remove the extra metal on top and leave only the electrode patterns. This is called the lift-off step. Following the lift-off process, we rinsed our sample in Acetone at 70 ^{0}C for 30 minute to remove any resist residue. The sample is then rinsed in IPA and dried with Nitrogen gas. The whole fabrication process is decribed by the flow chart in figure 2.3 and the final device in Figure 2.4.
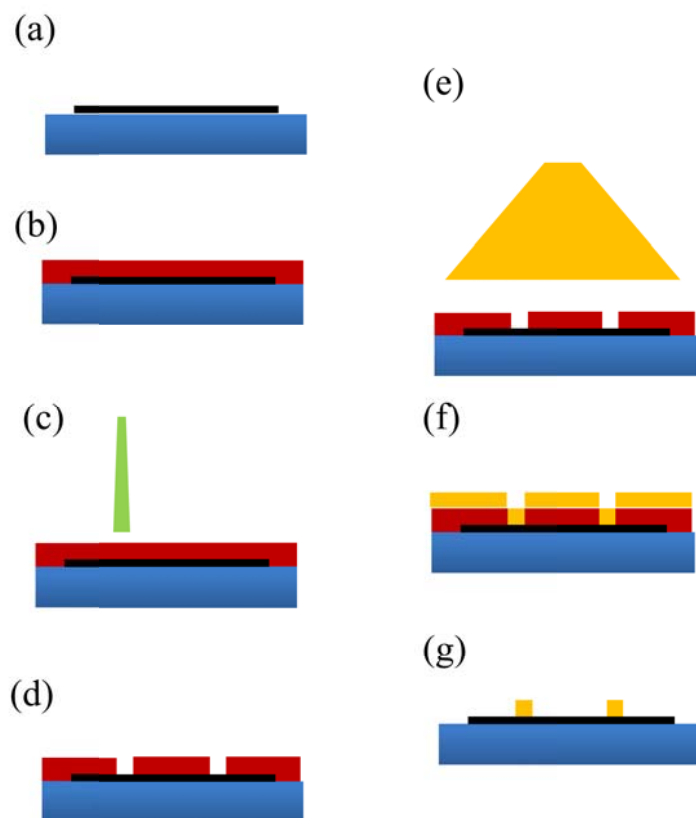
Figure 2.3 Device fabrication steps. (a) Exfoliate graphene onto Si/SiO$_2$ substrate. (b) Spin coat Bi-layer ebeam resist (MMA/PMMA). (c) Expose selected areas with electron beam. (d) Dip it into developer (IPA: MIBK = 3:1) for 80 Sec. (e)(f) Evaporate Ti(10nm)/Au (80nm) for contact electrodes. (g) Soak into PG remover at 70^{0}C until the ebeam resist is removed.
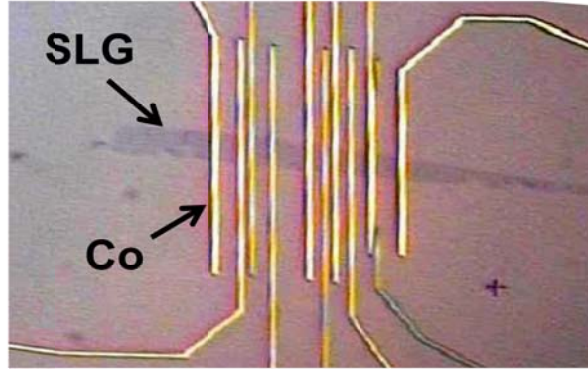
Figure 2.4 Ebeam pattern for single layer graphene (SLG) with 10 Co contact electrodes.

2.2: In-situ measurement.

2.2.1: Chamber System

In order to perform our experiments, we designed a chamber system to combine different functionality and capabilities. Figure 2.5 shows the top view drawing of the whole system. The system is comprised of different components; (1) Sample entry/exit, (2) LEED/Auger chamber, (3) STM Chamber with sample storage, (4) MBE with in-situ low temperature magneto-transport measurement system. (5) Conventional MBE system with ebeam and thermal evaporation cells.
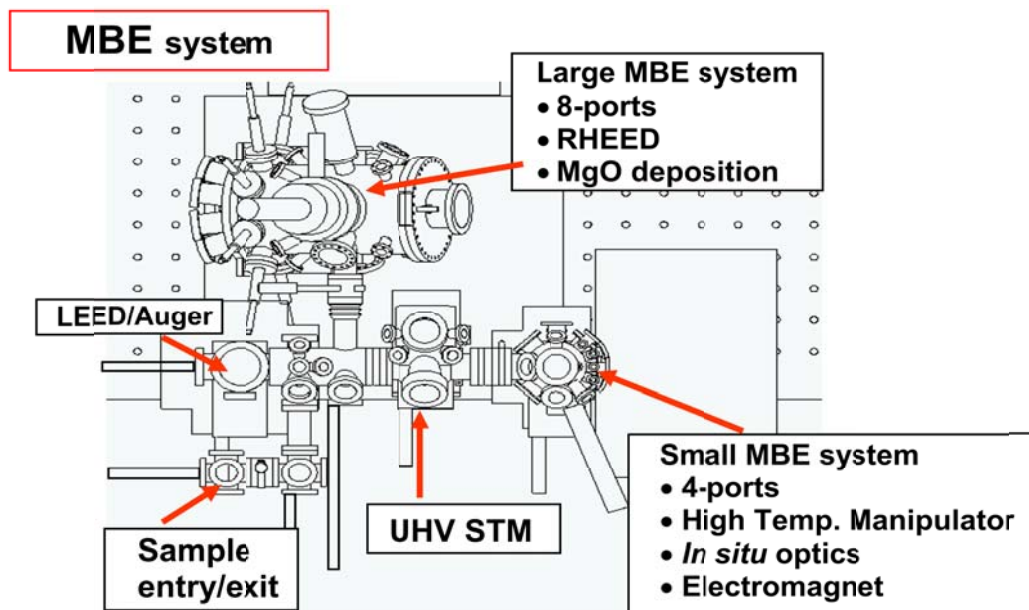
Figure 2.5 SolidWorks drawing of the chamber top view.

The sample load lock is the chamber designed for loading sample from atmosphere to ultra high vacuum (UHV). Sample was first mounted onto a specially designed paddle and loaded in the load lock chamber which is pumped out to a pressure below 5×10^{-6} torr or high vacuum. In order to prevent ruining the of UHV environments of both MBE systems, the samples are loaded into a buffer chamber which has pressures ranging from 5×10^{-7} to 1×10^{-9} torr. The buffer chamber helps prevent both MBE chamber from directly seeing the higher pressures and the water vapor from the load lock. The buffer chamber has a heater inside for which samples can be vacuum annealed up to 800^{0}C and a LEED/Auger measurement system for characterizing the basic material properties.

From the buffer chamber, the sample can be loaded into the large MBE chamber for materials deposition or into the small MBE system via STM chamber for *in situ* measurements combined with MBE capabilities. Before samples are measured, we anneal the completely fabricated device on the buffer heater at 150 ^{0}C for 1 hour to clean the sample[54]. After the annealing, the sample is ready to be measured and either can be stored in the STM chamber or/and loaded into the small MBE chamber for in-situ measurement.

2.2.2 Sample paddle set up and low temperature capability.

In order to measure samples inside the small MBE system, a special sample paddle was designed for in-situ electrical measurement and annealing the graphene devices [Figure 2.6b]. The paddle specially designed so samples could be mounted without the use of any glues or adhesives that could contaminate the UHV chamber. All the materials used for the sample paddle system are high temperature compatible, so it won't degas and contaminate the devices during annealing. Samples are mounted onto the paddle by spot wielding Ta foil to hold the sample in place. These sample paddles have an MgO bar with six Ti/Au contact pads on top for electrical contact. We wire bond our devices to the contact pads and contact electrical probe on these pads.
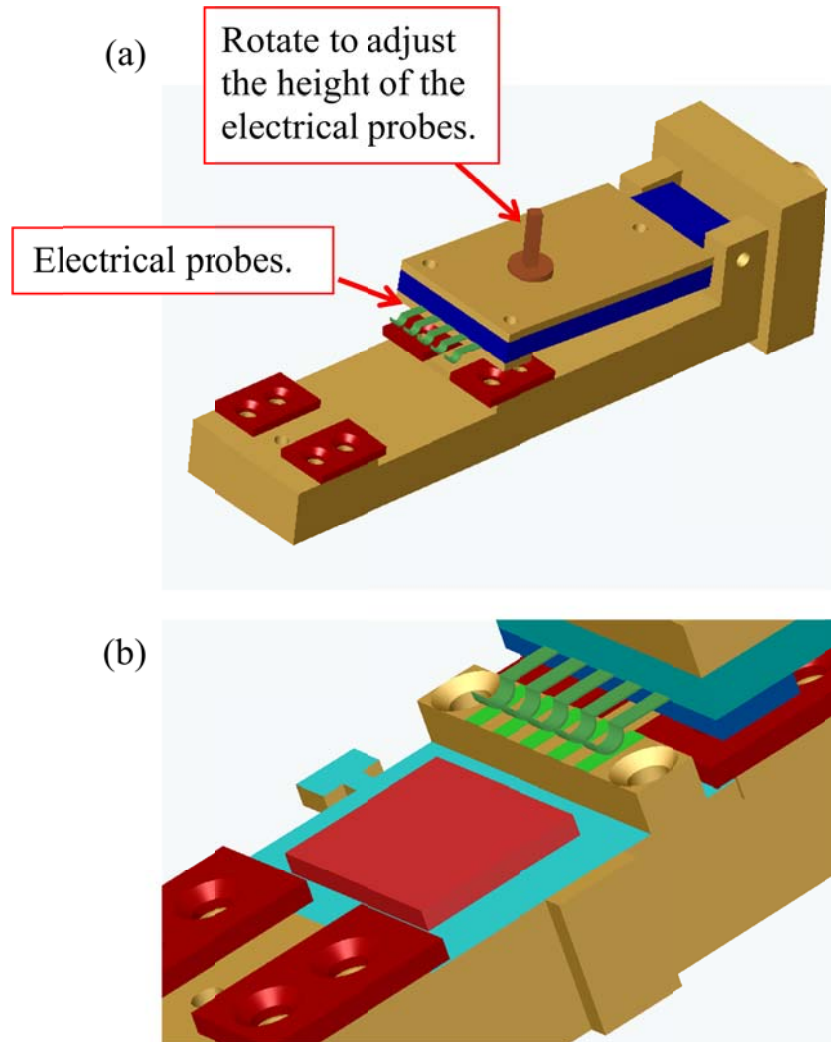
Figure 2.6 (a). SolidWorks drawing for Cu cold finger. The brown key is used to adjust the height of the electrical probes. The green probes are bent to provide some springing. (b). Picture of sample paddle in the measurement position.

The sample paddle is then transferred into the small MBE chamber and loaded onto the cold finger, which could be cooled down by an Advanced Research System helium flow cryostat system. On the cold finger there are six electrical pins that can be lowered to contact the electrode pads on the paddle by rotating the center key [Figure 2.6a]. During the lowering process, we monitored the position of probes through the CCD camera. Once the probes are close to the MgO bar, we apply a small voltage between two of the probe electrodes, which are aligned with two electrode pads that are purposely connected together. We check to see if there is any current between the two probes. If not, the voltage is then turned off, the probes are lowered more, then the small voltage is turned back on and the current is checked again. This process is repeated until we see a current flowing through the probes and indicating we are in contact with the electrode pads on the paddle. By doing this, we can avoid damaging the probes from lowing them too much turning the voltage off every time we lower the probes is necessary because leaving the voltage on may cause an arc between the sample and electrical probes and destroy the device.

We previously tried to directly contact electrical pads that were on SiO_2 wafer with the electrical probes. We found however, 300 nm of SiO_2 was too thin and the probes were able to easily punch through during the contacting process. This caused our devices to experience current leakage when we tried applying a back gate voltage. With the MgO bar design, we have the electrical probes making contact with a 0.5 mm thick MgO instead of 300 nm SiO_2, this prevent the gate leakage caused by the electric probe punching through the SiO_2 insulating layer.

The cold finger can cool down to 18 K with the constant Helium flow and a radiation shield. A Lakeshore 331 controller is used for feedback control the temperature leading to temperature fluctuation less than 50 mK. Once the sample is loaded inside the chamber, It can be rotated and moved into different positions for different purposes. It can be moved into position with the *in-situ* magnet for apply magnetic field measurements or moved into growth position for MBE deposition of materials to dope the sample.

2.2.3: Molecular beam epitaxial growth. (Cell design)

We designed two types of different types of evaporators for depositing materials to dope the graphene devices. First kind is the thermal effusion evaporator. The thermal cell works by heating a material high enough to the point it starts to evaporate. We use Ta or W wire to heat up crucible with our desired material inside causing it to evaporate the metal. With this designed, we are able to evaporate metal with melting point lower than the evaporation temperature. Biggest advantage is that the amount of metal we can have in each crucible is much more then, let say, for an ebeam evaporator. Therefore, the time between refills is much longer. Our crucible is wrapped by a piece of W or Ta wire and a thermocouple is located at the bottom of the crucible to monitor the temperature. By combining a Eurotherm temperature controller and a Sorensen power supply, we can control and stabilize the temperature of our cells to ±0.1 K [Appendix A2].

The second kind is ebeam evaporator, which uses an accelerated electron beam to heat up the target material to evaporate material. This is needed for materials that cannot

be evaporated with conventional thermal effusion evaporators. This design can evaporate materials with very high evaporation temperature, which are usually hard to grown. In our design, we passed current through the W wire to emit electron and apply 200 Volts on the grid to pull those electrons out toward the target metal. Target metals such as Ti and Pt are connected to a Glassman high voltage power supply which able to apply 600 W (5 kV, 120 mA) to the target [Appendix A].

For material growth rate, we have a quartz crystal deposition monitor inside the chamber to calibrate the rates before doping the sample with materials. The working principle of the quartz crystal deposition monitor is to monitor the oscillation frequency changes as the materials are deposited onto the quartz crystal and convert it to amount of material that has been deposited. With this deposition monitor, we were able to have the precise measurement of doping rate up to 0.01 Å/min.

2.2.4: Lock-in measurement with current source.

We use a lock-in amplifier to perform the electrical measurement in order to have better signal to noise ratio. Figure 2.7a is the schematic diagram of our measurement setup for our four-probe resistance measurement. We take the modulated voltage signal from the lock-in amplifier and send it into the home-made current source [Appendix B] to convert the voltage to current. This oscillating current is sent between electrode A to D and we probe the voltage difference between electrode B and C using a Stanford SR560

voltage amplifier. This signal is sent back into the lock-in amplifier and converted to voltage.

For the back gate voltage, we add a protection circuit before we connect to the device (figure 2.7b). This protection circuit can avoid a rapid voltage change by ramping the Keithley 2400. A rapid voltage change will cause a huge current pulse and this could easily damage the device. Our voltage ramp rate is usually 10 ms/step, therefore we pick resistor of 1 kΩ and capacitor of 0.47 μF to make sure the time constant is not too long. In this case, we can have our set voltage reached the maximum value before Keithley 2400 changes to the next voltage.
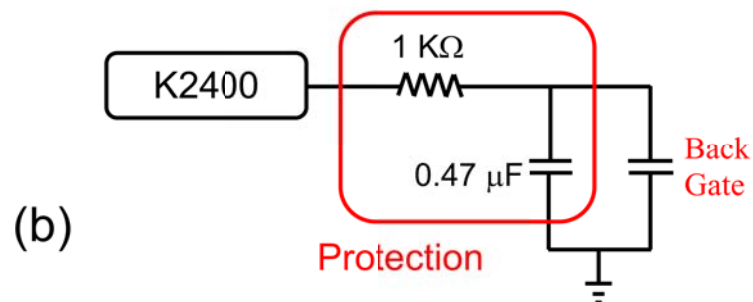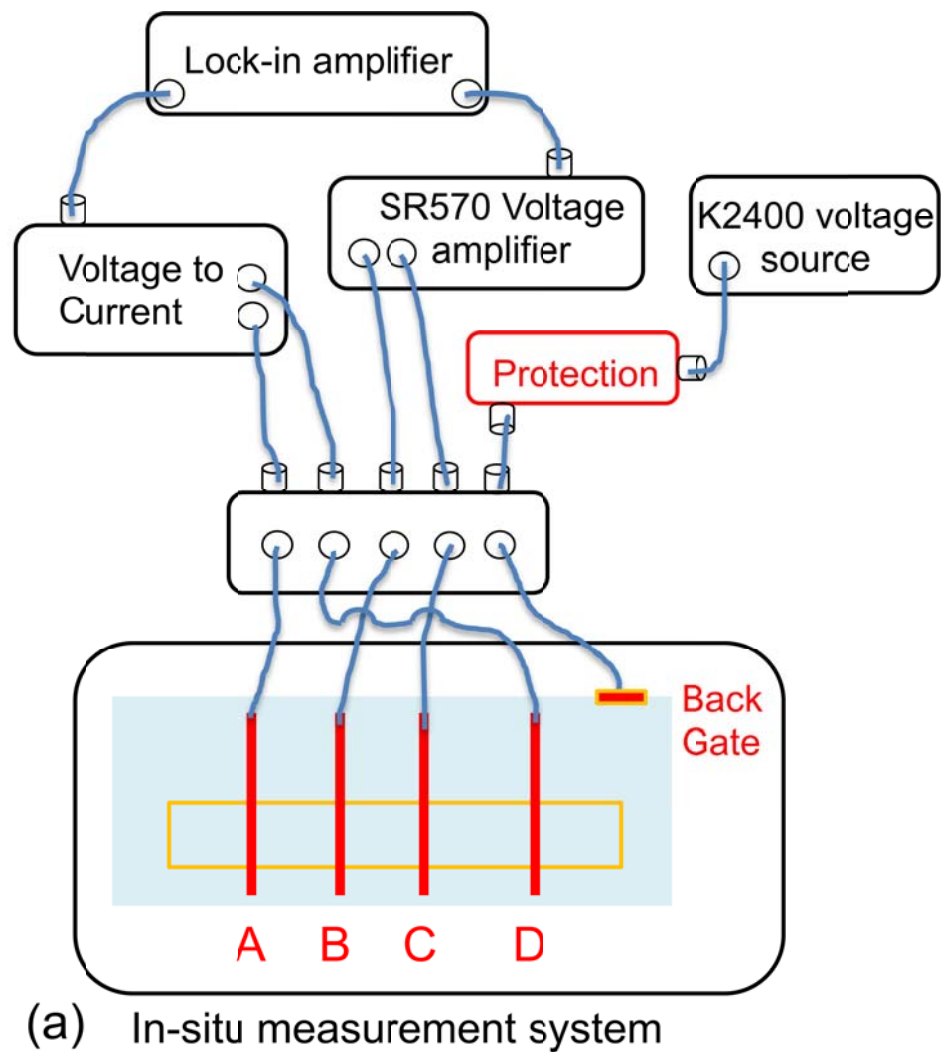
Figure 2.7 (a) The schematic diagram for 4-probe measurement setup. (b) RC protection circuit.

2.3: Introduction of Non-local spin valve measurement.

The measurement technique we use is called the non-local magnetoresistance measurement. In order to better understand this measurement, we first introduce the local magneto-resistance measurement. Figure 2.8 shows the schematic diagram of spin valve measurement. We inject spin polarized current from ferromagnet (FM) into graphene. The spins are then driven across the graphene by the bias voltage and are detected by the second FM electrode. In our study, we use Co as ferromagnetic electrode, which has 34% spin polarization at room temperature. This can be understood in terms of resistance circuit. When we have parallel geometry for both FM electrodes, it acts as a high resistance channel connected in parallel with a low resistance channel. In contrast, when we have anti-parallel geometry, high resistance channel connected in series with the low resistance channel. Local magnetoresistance can be defined as equation 2.1.

$$\frac{\Delta R}{R} = \frac{R_{AP} - R_P}{R_{AP}} = \frac{2p_1 p_2 e^{-L/\lambda_G}}{1 + p_1 p_2 e^{-L/\lambda_G}} \qquad (2.1)$$

Where $\Delta R/R$ is the channel width (L) dependent magnetoresistance, R_{AP} and R_P is the resistance for anti-parallel and parallel configurations, respectively, p_1 and p_2 are the spin polarization for FM1 and FM2, and λ is the spin diffusion length. This calculation considers the spin relaxation in graphene by multiplying an exponential decay term (e^{-L/λ_G}) to p_1 for the polarization lost after transport through channel L.
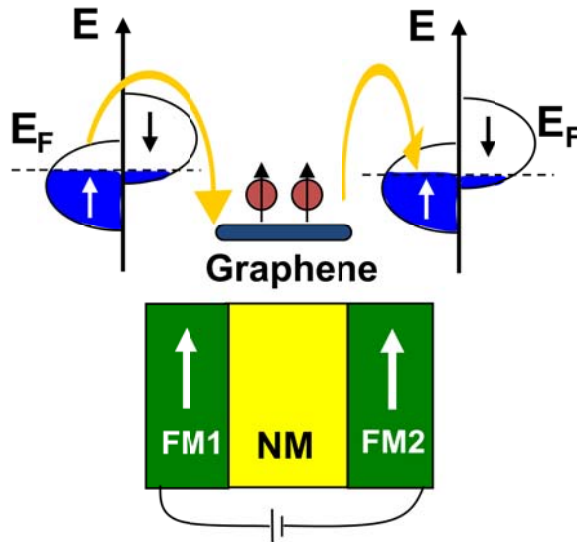
Figure 2.8 Schematic diagram of spin valve in (a) low resistance state (parallel geometry) and (b) high resistance state (anti-parallel geometry).

For nonlocal measurement, the basic idea of different resistance state for parallel and anti-parallel geometry is the same. The difference is nonlocal measurement has no net current flow through the transport channel and has only spin current diffuse through it. Therefore, this measurement won't detect the background resistance and is only sensitive to the resistance change due to the spin dependent transport. The non-local MR is defined as $\Delta R_{NL} = R_{NL}^P - R_{NL}^{AP}$, where R_{NL}^P (R_{NL}^{AP}) is the non-local resistance for the parallel (anti-parallel) state.

Quantitatively, the one-dimensional drift-diffusion theory of spin transport derived by Takahasi and Maekawa [55], where R_{NL} is given by equation 2.2. Derivation for this equation is in Appendix C.

$$R_{NL} = \frac{V_2}{I} = 2R_N e^{-L/\lambda_N} \prod_{i=1}^{2} \left(\frac{P_J \frac{R_i}{R_G}}{1 - P_J^2} + \frac{P_F \frac{R_F}{R_G}}{1 - P_F^2} \right)^2 \times \left[\prod_{i=1}^{2} \left(1 + \frac{2\frac{R_i}{R_G}}{1 - P_J^2} + \frac{2\frac{R_F}{R_G}}{1 - P_F^2} \right)^2 - e^{-2L/\lambda_G} \right]^{-1} \quad (2.2)$$

The parameters P_F and P_J are the spin polarization of the FM and Junction, R_i, R_F and R_G are the contact resistance between the FM and SLG, FM electrode resistance and graphene resistance, respectively. We take the limit of $R_i << R_G$ to descript the transparent contact regime which is the type of device we use in later studies. We will get equation 2.3

$$R_{NL} = 4R_N e^{-L/\lambda_G} \frac{\left(\frac{P_F}{1 - P_F^2} \right)^2 \left(\frac{R_F}{R_G} \right)^2}{1 - e^{-L/2\lambda_G}} \quad (2.3)$$

In this equation, we can see that the R_{nl} is proportional to the graphene conductivity Therefore, gate dependent R_{NL} should follow the trend of gate dependent conductivity for transparent contact non-local spin valve devices.

Chapter 3:

Electronic properties of graphene with transition metal doping.

3.1: Introduction.

Transition metal (TM) adatoms and clusters on graphene have recently been a topic of great interest: at low density, they are expected to induce doping, scattering [56], and novel magnetic [57-59] and superconducting [60] behavior; at high density (up to continuous coverage), they may locally dope or modify the band structure of graphene [61-63]. Because of their importance for graphene-based electronics and the investigation of novel phenomena [56-69], there have been extensive theoretical studies [56-63, 68, 69]. In contrast, the experimental exploration of TM/graphene systems is much more limited.

The discussion in this chapter is going to mainly focus on two effects caused by TM doping on graphene. We first studied the charge transfer mechanism between transition metal and graphene and then identify which kind of charge scattering mechanisms has the dominant effect when we add TM adatoms onto graphene.

The charge transfer between the TM and graphene is a key issue to investigate because it is responsible for both the local doping and the charge impurity scattering. Generally, the relative work function (WF) between the TM and the graphene is believed to be important factor for determining the charge transfer [66], *i.e.* graphene will be *p*-doped (*n*-doped) if the TM's WF is larger (smaller) than graphene. Recently, there are some experimental papers used photocurrent to study doping between electrodes and graphene.

The TMs that have been used in these previous studies are Ti, Au and Cr which are the most commonly used metals for electrode contact[65, 67]. These experimental results agreed with the WF model if we compare them with the theoretical calculated graphene work function. For example, we have Ti bulk work function ~ 4.3 eV[70] and we have graphene work function ~ 4.5eV[71, 72]. Therefore, we will expect *n-type* doping from Ti electrode making contact to the graphene flake. However, these previous results weren't able to explain the presence of a strong interfacial dipole that promotes the *n-type* doping of graphene predicted by density functional calculation[65-67, 73]. In this chapter, we will discuss the theory and experimental result for evidence of interfacial dipole between TM and graphene.

3.2: Device preparation (ebeam pattern, electrode, sample cleaning).

We start the device fabrication with our standard exfoliation and ebeam lithography process [chapter 2]. To match our purpose of the study, we use Temescale BJD ebeam evaporator system to deposit 8 nm of Ti as adhesion layer and 100 nm of Au on top for electrode contact. Figure 3.1 shows a scanning electron microscope (SEM) image and optical microscope image of a typical graphene device with Au/Ti electrodes defined by e-beam lithography. In order to have a clean starting point for our study, the devices are annealed under Ar/H_2 environment in the Fisher scientific tube furnace at 200°C for one hour to remove resist residue[54, 74]. To prevent any damage to the electrodes from the annealing step, thick Au electrodes are essential. After the hydrogen annealing, we anneal

the device again in ultrahigh vacuum at 90°C for one hour to remove the water and gas that might have been absorbed by the clean graphene surface during the transferring of device to UHV chamber system.
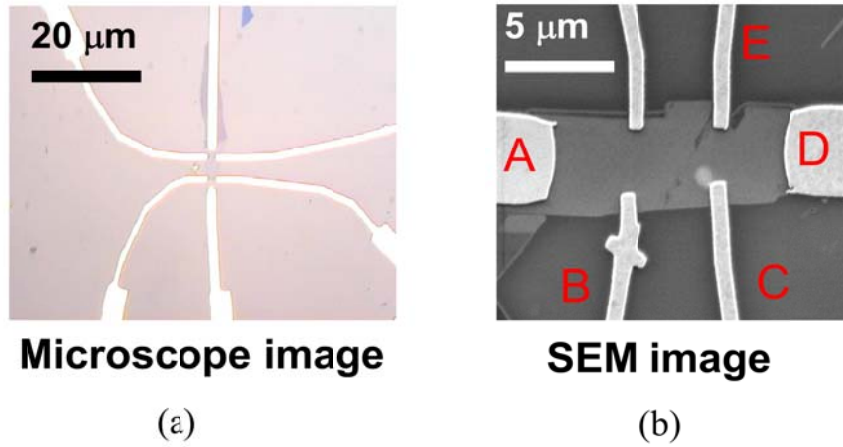
Figure 3.1 (a). Optical microscope and (b). SEM images of Hall bar device geometry.

3.3: Electrical properties of graphene.

Graphene has fantastic electronic properties. For carbon material expect diamond, π electrons are the electrons that contribute to the charge transport. Therefore, to understand the electronic properties of graphene we can calculate the π band by using tight binding model. Consider the contribution from nearest neighbor and the equivalent of A and B site [Figure 3.2a], we can calculate the Hamiltonian and get the eigenvalues E (k_x,k_y) [equation 3.1][Appendix D] [75].

$$E_{g,2D}(k_x, k_y) = \pm t \left\{ 1 + 4\cos\left(\frac{\sqrt{3}k_x a}{2}\right) \cos\left(\frac{k_x a}{2}\right) + 4\cos^2\left(\frac{k_x a}{2}\right) \right\}^{1/2}$$

(3.1)

This equation shows the upper π band and the lower π band are degenerate at the K point where the Fermi energy passes. This is called the dirac point. Because of this unique band structure, graphene is a zero-gap semiconductor [Figure 3.2b]. We are able to tune the carrier concentration and carrier type by tuning the back gate voltage to modify the Fermi level.

(a)   (b)
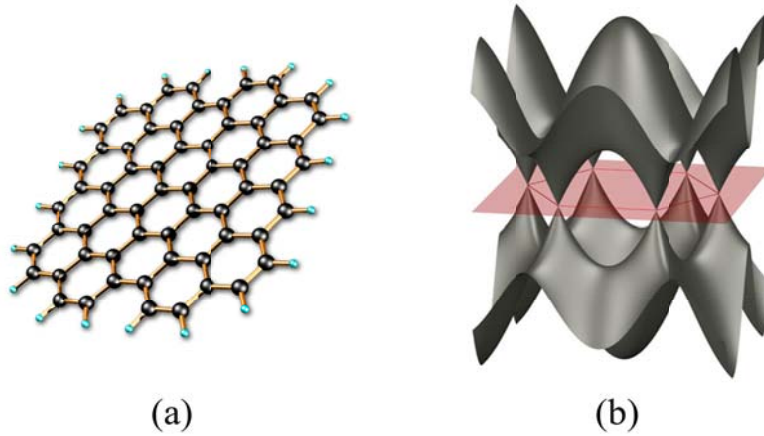
Figure 3.2 (a). Graphene structure: black spheres are the carbon atoms and blue spheres are the hydrogen that bonds to the graphene edge. (b). Energy dispersion of 2D graphene along the high symmetry direction

Figure 3.3 shows the gate dependent conductivity of our graphene Hall bar device. We passed current from A to D and measured the voltage from B to C [see Figure 3.1b] for longitudinal resistance. For transverse resistance, we applied current from A to D and measured the voltage between C and E.
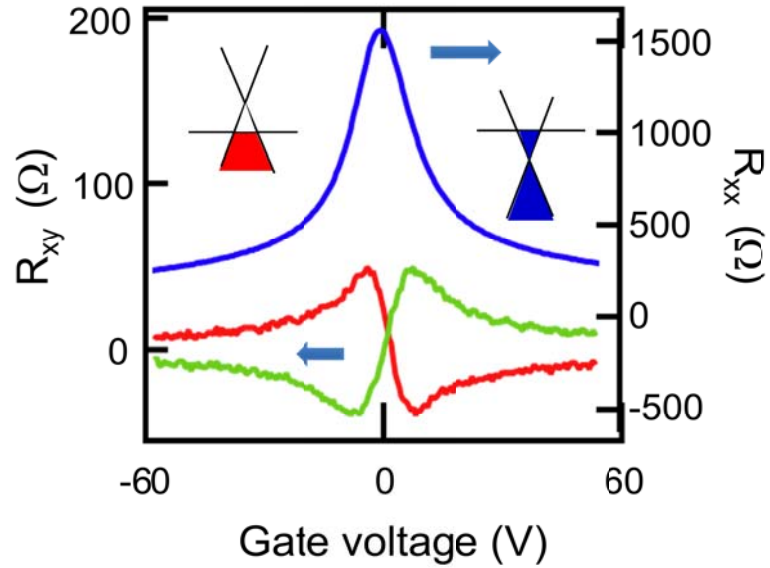
Figure 3.3 Gate dependent longitudinal resistance (blue curve) and gate dependent transverse resistance (green and red curves) (B field = 1070 Oe). Insets are the Dirac cone and Fermi level for electron transport regime (blue) and hole transport regime (red).

This four probe measurement allows us to measure only the resistance change in graphene without detecting the resistance of interface and electrodes. By tuning the gate voltage, we are able to change the carrier concentration depending on equation

$n = \alpha(V_g - V_D)$, where n is the carrier concentration, α is a constant related to the dielectric constant of 300 nm of SiO_2, V_g is the applied gate voltage and V_D is the original dirac point. In our case, $\alpha = -7.2 \times 10^{10}$ $V^{-1}cm^{-2}$ based on calculated capacitance values of SiO_2 for 300 nm thick. Due to the special band structure, we should observe minimum conductance at the Dirac point [Figure 3.3]. This minimum conductance came from the contributions of the carrier by thermally excited or charged impurities on the surface. For example, the minimum conductance for suspended graphene after thermal annealing treatment can be much lower and also the position of the peak could be much closer to the zero gate voltage after removed most of the charged impurities from graphene[12, 76]. Later in the study, we also use relative Dirac point position as a indicator for the amount of impurities we added on top of graphene.

3.4: Experimental detail.

To understand the charge transfer mechanism between TMs and graphene, we doped graphene with MBE technique. With the sample inside UHV, electrical properties can stay for months without changing under the clean environment. The room temperature MBE deposition of TM atoms (growth pressure $< 7 \times 10^{-10}$ torr) is calibrated by a quartz deposition monitor. The fine control of TM deposition provides the ability to probe the effect of small amounts of material on the transport properties of graphene. The coverage is converted from atoms/cm^2 to "monolayers" (ML) where 1 ML is defined as 1.908×10^{15} atoms/cm^2, the areal density of primitive unit cells in graphene.

For low coverage, the room temperature deposition of TM leads to clustering as shown in the atomic force microscope (AFM) image of 0.62 ML Pt on graphene [figure 3.9b]. Dependence on different materials, some diffusion barrier for TM move on graphene can be overcome by the thermal energy. For Ti, Fe and Pt that was used in this study, we observed clustering effect on all of them. Limiting by our AFM resolution, the presence of isolated adatoms cannot be ruled out, but are unfavorable theoretically [61, 77]. In chapter 3.5.4, we will have more detail discussion about this clustering effect.

For electrical measurement, *in-situ* transport measurements are performed using standard lock-in detection (1 µA excitation) [Chapter 2.4].

3.5: Result.

3.5.1: Doping graphene by TM with different work function.

We first doped graphene with Ti which has bulk work function ~ 4.3 eV. Graphene, which has theoretical calculated work function 4.5 eV, was expecting to receive *n-type* doping from Ti. Figure 3.4a shows representative gate dependent conductivity scans for various thicknesses of Ti in the low coverage regime. The minimum in the gate dependent conductivity identifies the position of the Dirac point (V_D), while the slope corresponds to the mobility of charge carriers in the graphene. With increasing coverage, two characteristic behaviors are observed. First, the introduction of Ti on the graphene surface results in shifting the Dirac point towards more negative gate voltages, indicating

that the Ti is a donor, producing *n-type* doping in the graphene [Figure 3.4b]. Second, the slope of the conductance curves away from the Dirac point decreases, indicating that the Ti introduces additional scattering to lower the mobility. For the present of additional scattering with the increasing amount of TM coverage will be discussed in the later section 3.5.
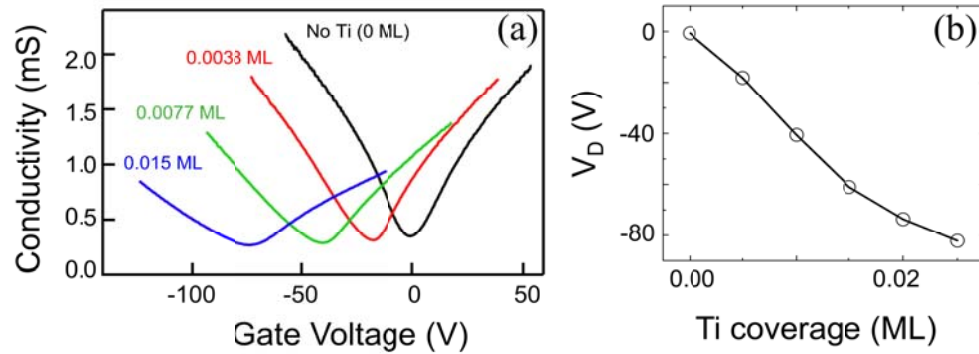
Figure 3.4 (a). Gate dependent conductivity curves for different Ti coverage.
(b). Dirac point vs. Ti coverage.

Fe, with bulk WF ~ 4.7 eV, which is slightly higher than work function of graphene, expected to give graphene *p-type* doping if work function is the only mechanism that determine the doping of graphene. However, we observed *n-type* doping when we deposited Fe on graphene as well. The Dirac point also shifted to the left but with doping effect lot weaker compare with Ti [Figure 3.5].
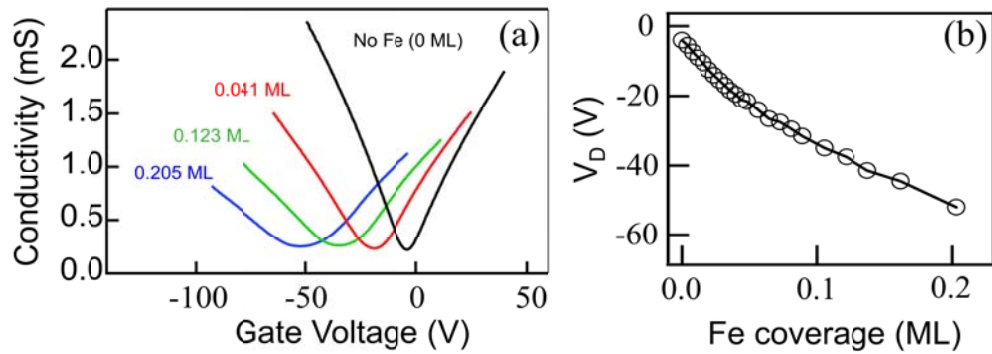
Figure 3.5 (a). Gate dependent conductivity curves for different Fe coverage.
(0 ML, 0.041 ML, 0.123 ML, 0.205 ML) (b). Dirac point vs. Fe coverage.

In order to see if it is possible to achieve *p-type* doping with low coverage of TM deposition and understand if there is clear trend with work function. We deposited Pt (bulk work function ~5.9eV), which has the highest work function of all the material we can have avaliable. Surprisingly, Pt still gives us slightly *n-type* doping [Figure 3.6]. This result suggests a different mechanism plays an important role other than just simply compare the work function.
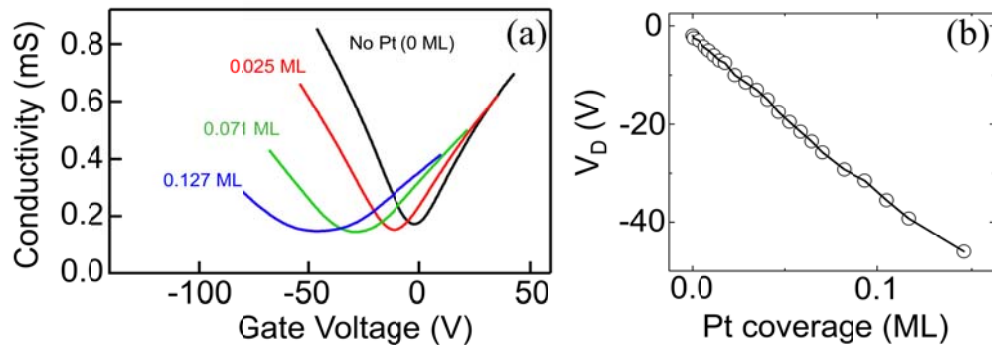
Figure 3.6 (a). Gate dependent conductivity curves for different Pt coverage.
(0 ML, 0.025 ML, 0.071 ML, 0.127 ML) (b). Dirac point vs. Pt coverage.

Figure 3.7 highlights the relation between the Dirac point shift ($V_{D,shift} = V_D - V_{D,initial}$)

and TM coverage for a collection of Ti, Fe, and Pt samples in the low coverage regime.

Here we show our result for all night samples. Despite the sample-to-sample variations

which may be due to differences in the graphene surface purity, growth rate uncertainties,

and the possible dependence of graphene WF on flake size or edge roughness [78],

several important features are discovered. First, for all samples, including the Pt samples

with Pt WF greater than graphene, result in *n-type* doping. Second, the three different TM

results in three different slope ranges, with the Ti samples exhibiting the most negative

initial slopes (-2169 to -4602 V/ML). From this value the doping efficiency, or number of

electrons transferred per Ti atom to graphene is determined by knowing the carrier

concentration associated with the given change in gate voltage ($\Delta n = \alpha \Delta V_g$, where α

$= 7.2 \times 10^{10}$ $V^{-1}cm^{-2}$ based on calculated capacitance values). The doping efficiency is in

the range of 0.082 to 0.174 electrons per Ti atom. The Fe shows the next strongest

efficiency (0.017 to 0.046), while the Pt is the weakest electron donor with the efficiency

of 0.014 to 0.021 electrons transferred for each Pt atom. Upon recalling the bulk WFs of

Ti (4.3 eV), Fe (4.7 eV), and Pt (5.9 eV), it is apparent that the WF of the TM directly

affects the doping efficiency, with electrons being more easily transferred from the

lowest WF material, Ti, compared to the highest WF material, Pt. Although the WF of Fe

is much closer to that of Ti, the doping efficiency of Fe is more similar to that of Pt. This

behavior implies that in addition to the work function, wave function hybridization,

structural modifications, or other effects may contribute to the electronic doping of

graphene.
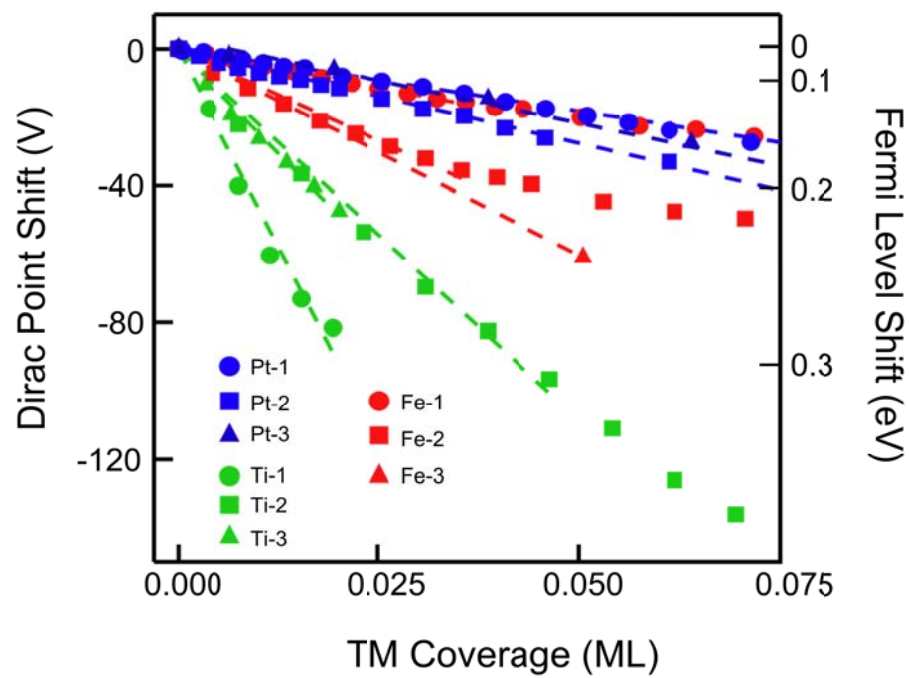
Figure 3.7 Summary plot of Dirac point shift vs. TM coverage for Ti, Fe and Pt.

3.5.2: Experimental evidence of interfacial dipole between transition metal and graphene.

In previous section, an unexpected result from the studies at low coverage (section 3.4.1) is the *n-type* doping of graphene by Pt. If the WF is the only factor affecting the transfer of electrons between materials, Pt is expected to dope graphene strongly *p-type*, since the WF of Pt (5.9 eV) is significantly larger than that of graphene (4.5 eV). Density functional calculations of bulk TM on graphene [63] present a possible explanation for this observed behavior by predicting the formation of an interfacial dipole layer, resulting in a potential step to favor *n-type* doping.

This potential step given in this theory can be written as $\Delta V(d) = \Delta_{WF}(d) + \Delta_c(d)$, where $\Delta_{WF}(d)$ results from the charge transfer due to the work function different between TMs and graphene and $\Delta_c(d)$ is from the short range wave function hybridization between TMs and graphene.

$$\Delta_c(d) = e^{-\gamma d}\left(a_0 + a_1 d + a_2 d^2\right)$$

(3. 2)

Equation 3.2 show that $\Delta_c(d)$ is highly dependence with the d and the strength is exponentially decay if we increase the distance[50]. Figure 3.8 shows the schematic band diagrams when transition metal brought in contact with graphene. W_M is the work function for TMs (Ti~4.3 eV, Fe~4.7 eV and Pt~5.9 eV), W_G is the theory calculated graphene work function (~4.5 eV), ΔV is interfacial dipole, d is the distance between transition metal and graphene, E_F is the Fermi level, W is the graphene work
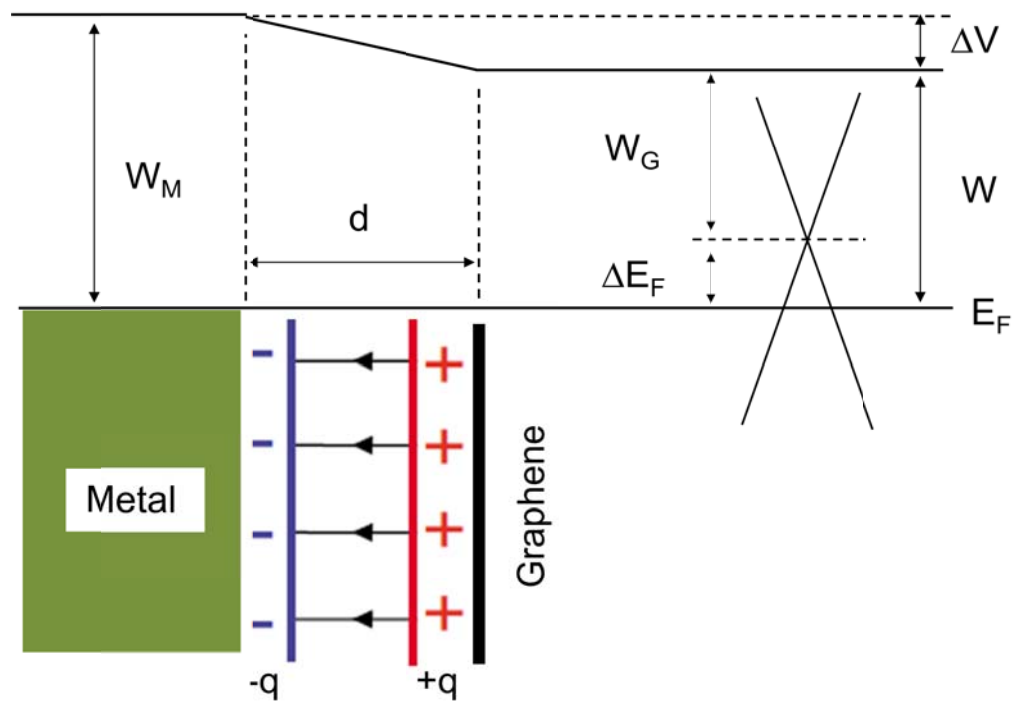
Figure 3.8 Schematic diagrams of the interfacial dipole and potential step
formation between TMs and graphene[50, 79].

function after the metal coverage, and ΔE_F is the differences between W and W_G. By changing the d between graphene and TM, $\Delta_c(d)$ can be larger while $\Delta_{WF}(d)$ keep the same. Therefore, $\Delta V(d)$ can be increase. As we can see the expression in figure 3.7b, because ΔV enhance but W_G stay the same, ΔE_F could turn negative. That makes the *n-type* doping possible even when W_M is originally bigger than W_G.

So far, however, there has been no experimental evidence for such a strong dipole layer forming at the interface between a bulk TM and graphene [64-67]. To investigate the theoretical prediction of a strong interfacial dipole layer between the graphene and bulk TM, we extend the Pt-doping study to higher coverage to study the charge transfer from Pt films.

Figure 3.9a displays V_D as a function of coverage for several Pt-doped samples. An initial rapid shift toward negative voltages is observed in all samples. As more Pt is deposited, bringing the sample into the medium coverage regime, the rate of shift in V_D slows and reaches a minimum value before gradually increasing towards more positive voltages. At high coverage, the Dirac point stabilizes and shows very little variation with additional deposition. The sample morphology is measured by *ex situ* AFM. The AFM image for 0.62 ML of Pt shows that the Pt is still in the form of isolated clusters (Figure 3.9b). At the higher coverage of 3.19 ML, the Pt forms a connected film with some uncovered regions of graphene (Figure 3.9c). The connected film provides a parallel conduction pathway that contributes to the measured conductivity value, but should not be gate dependent. The gate dependence of the conductivity is primarily due to the
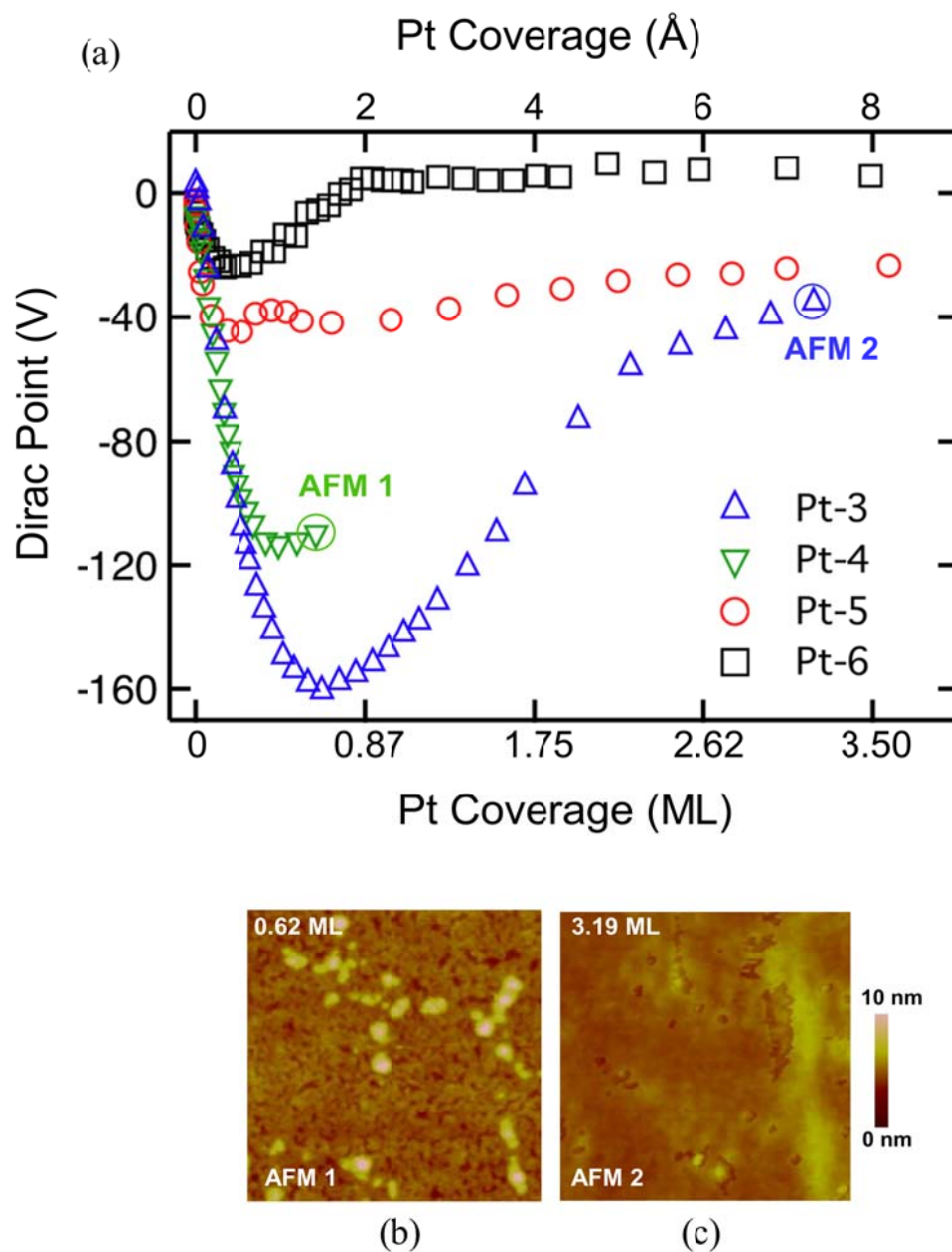
Figure 3.9 (a). The Dirac point as a function of Pt coverage up to high coverage. (b). AFM image of 0.62 ML Pt exhibits isolated clusters. (c). AFM image of 3.19 ML Pt indicates a connected film with some areas of bare graphene.

chemical potential shift of the graphene that is not covered by the metal. For graphene in direct contact with metal, the local chemical potential is pinned, exhibiting no gate dependence. Transport measurements provide a reliable method for determining the V_D as well as the type of doping (electron or hole) in the uncovered graphene regions for both the clusters and the partially covered films. Thus, the final values of V_D in the high coverage regime clearly show that Pt films can produce either *n-type* or weak *p-type* doping of the graphene. This sample-to-sample variation is most likely due to differences in the initial surface purity among samples. Although hydrogen cleaning is performed on all samples, trace amounts of resist residue could remain, directly affecting the TM-graphene spacing. For example, with dirtier sample, it is possible the resist residue will act as spacer and increase the *d* between TMs and graphene.

The equilibrium distance change between TMs and graphene while the coverage went from individual adatoms to continuous film could explain this switch back behavior. Based on theoretical calculations, the *d* between TM adatoms and graphene is less than 3 Å [61] while for bulk TM the distance increases to ~3.3 Å [63]. The *n-type* doping observed in samples at low coverage is an indication of a strong interfacial dipole favoring *n-type* doping, as expected for low coverages exhibiting a small d_{eq}. As the bulk-like regime is approached, the increasing d_{eq} decreases the dipole strength and hence reduces the *n-type* doping efficiency as observed by the shift in the Dirac point toward positive voltages. Due to the highly spacing-dependent interfacial dipole strength, any variations in the spacing will directly affect the type and amount of doping. The fact that both *n-type* and weak *p-type* doping is observed provides experimental evidence for the

presence of a strong interfacial dipole layer favoring *n-type* doping as predicted theoretically [63] because the expected doping based only on WF considerations would lead to strong *p-type* doping.

We emphasize that the interfacial dipole provides just one possible scenario to explain the non-monotonic evolution of the Dirac point shift. A quantitative understanding is complicated by the fact that the WF can differ from bulk values for small clusters (< 4 nm lateral size) [80] and the corresponding quantity for adatoms (should they be present) is the first ionization energy. Therefore, further theoretical calculations are needed to fully understand the doping effect of clusters. Regardless of the exact mechanism for doping by clusters, an interfacial dipole is still necessary to explain the *n-type* or weak *p-type* doping measured in the bulk-like regime.

3.5.3: Theory of charge transport in graphene.

There are many different type of charge scattering mechanism in graphene; such as charged impurities (ci), short-range scatters(sr), acoustic phonons (p), surface ripple (r) and mid-gap state (mg) (equation 3.3).

$$\sigma^{-1} = \sigma_{ci}^{-1} + \sigma_{sr}^{-1} + \sigma_{p}^{-1} + \sigma_{r}^{-1} + \sigma_{mg}^{-1}$$

(3.3)

For all the experimental data, graphene conductivity is proportional to the carrier concentration at low carrier concentration region and show sub-linear behavior at higher concentration [19, 22]. These observations agree with the theoretical prediction that

Graphene conductivity should be linearly dependent to the carrier concentration if the dominant scattering mechanism is the charged impurities, as equation 3.4. Where C_{ci} is a constant calculated by using random phase approximation to model the screened Coulomb potential, n_{imp} is the density of charged impurities, and e is the electronic charge.

$$\sigma_{ci}(n) = C_{ci} e \left| \frac{n}{n_{imp}} \right|$$

(3.4)

From the previous section (3.4.1), we realize a significant amount of charge transferring when TMs brought in contact with graphene. Therefore, we want to investigate the type of scattering mechanisms that have been introduced by the TMs doping.

3.5.4: Charge scattering induced by transition metal doping.

Figures 3.10 a-c show the conductivity as a function of carrier concentration [$n = -\alpha(V_g - V_D)$]. The electron and hole mobilities are determined by taking the slope of the conductivity away from the Dirac point ($\mu_{e,h} = |\Delta\sigma/e\Delta n|$) [19, 81]. Figures 3.10 d-f illustrate the detailed dependence of mobility on the TM coverage for Ti, Fe, and Pt samples in the low coverage regime. Comparing the different samples at equivalent coverages, the Ti exhibits the strongest scattering and Pt has the weakest scattering.
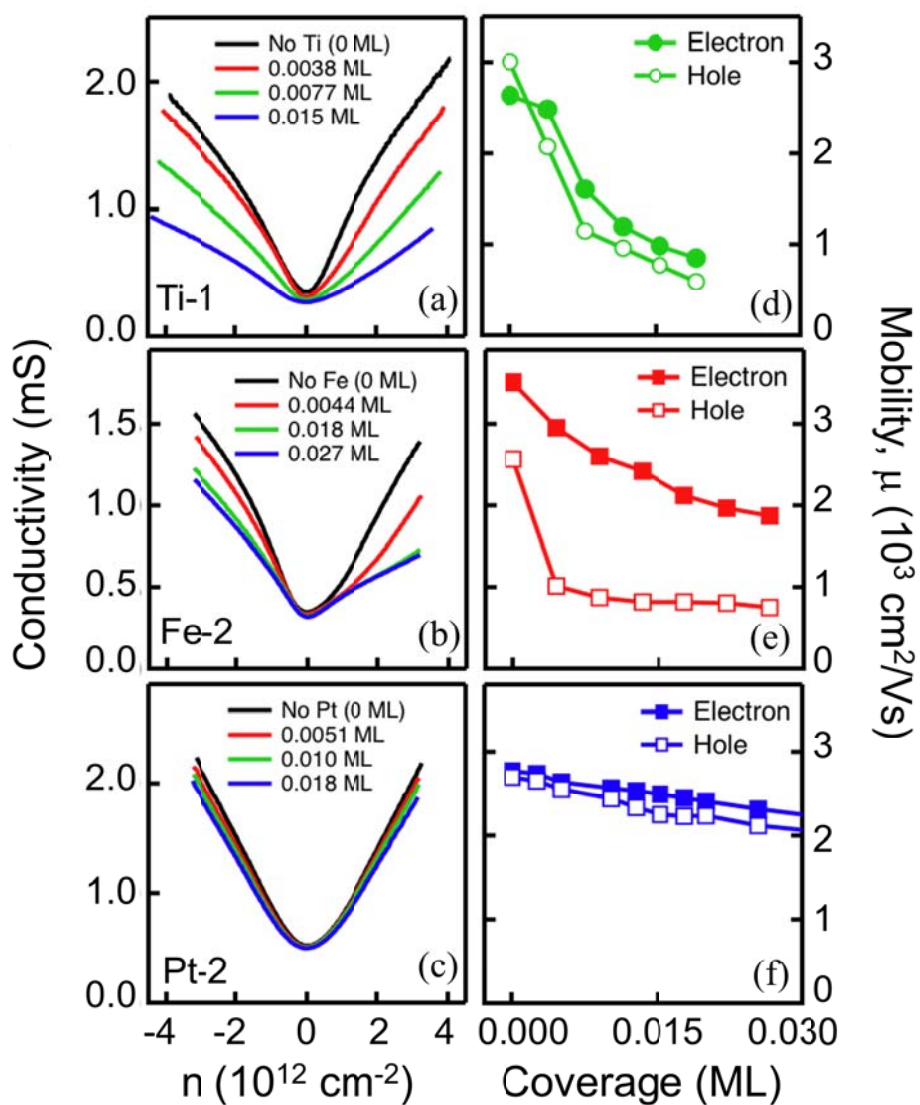
Figure 3.10 (a-c) The conductivity vs. carrier concentration for Ti, Fe, and Pt, respectively, for four different TM coverages. (d-f) The electron and hole mobilities for Ti, Fe, and Pt, respectively, as a function of TM coverage.

Noting that the trend in the scattering (Ti > Pt) matches that of the doping efficiency, we investigate this relationship by plotting the normalized mobility [82] against the Dirac point shift (Figure 3.11). The average mobility, $\mu = (\mu_e + \mu_h)/2$, is plotted for Ti and Pt. The Fe samples typically exhibit a reduction of hole mobility which is most pronounced in sample Fe-2, so μ_e and μ_h are plotted separately. Comparing the different materials shows that the mobility reduction of Ti, Pt, and Fe (electrons) is much more strongly related to the Dirac point shift than the TM coverage (Figure 3.11).
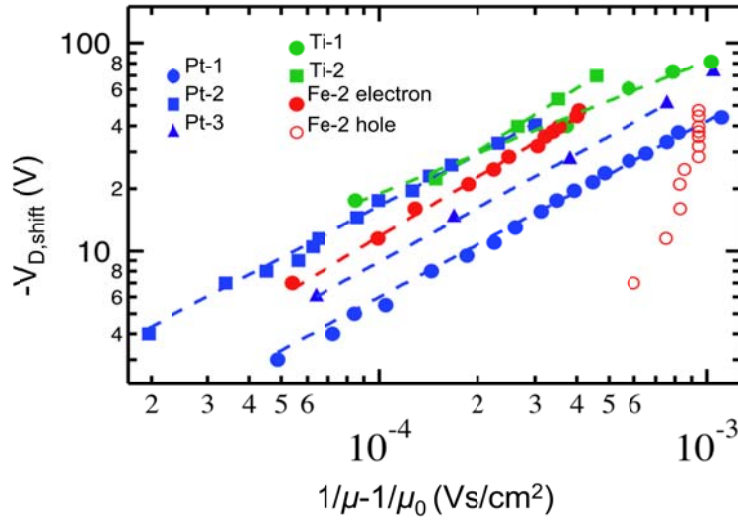
Figure 3.11 $-V_{D,shift}$ is plotted vs. $1/\mu - 1/\mu_0$. The dashed lines are power law fits to the equation, $-\Delta V_{D,shift} \sim (\Gamma_{TM})^b$ where b is 0.64, 1.01, 0.85, 0.83, 0.86 and 0.95 for Ti-1, Ti-2, Pt-1, Pt-2, Pt-3 and Fe-2 electrons, respectively.

Because the Dirac point shift not only measures the doping level in the graphene but also the average charge density of the TM, the data shows that the scattering is related to

the average charge density of the clusters—a characteristic that is plausible for Coulomb scattering. However, we point out that this behavior is actually different from what is calculated for Coulomb scattering by point-like scatterers with $1/r$ potential [83]. Specifically, in ref. 26, the scattering per impurity does not scale linearly with the impurity charge (α_ε) and instead has a strong quadratic component, resulting in scattering that scales as $\alpha_\varepsilon^2 n_{imp} = \alpha_\varepsilon(\alpha_\varepsilon n_{imp}) \sim \alpha_\varepsilon(V_{D,shift})$. Due to the presence of the material-dependent α_ε factor (i.e. doping efficiency), the mobility vs. Dirac point shift curves should be significantly different for different materials. Therefore, the observed scattering by TM clusters exhibits behavior that differs from $1/r$ Coulomb scattering by isolated impurities [56].

Additionally, we analyze the power law relationship between the scattering and doping effects. The total scattering rate is $\Gamma = \Gamma_0 + \Gamma_{TM}$, where Γ_0 is the scattering rate of the undoped sample and Γ_{TM} is the scattering rate induced by the TM. Because mobility is inversely proportional to scattering, the quantity $1/\mu - 1/\mu_0$ is proportional to Γ_{TM}. The relationship between the Dirac point shift and Γ_{TM} is investigated by plotting $-\Delta V_{D,shift}$ vs. $1/\mu - 1/\mu_0$ on a log-log scale (Figure 3h). The dashed lines are power law fits, $-\Delta V_{D,shift} \sim (\Gamma_{TM})^b$, with values of b ranging from $0.64 - 1.01$ as indicated in the figure caption. Compared to the results of Chen et. al. [19] which find values of $b = 1.2$-1.3 for scattering by isolated potassium impurities, our results with $b \leq 1$ indicate a different behavior for scattering by TM clusters.

3.6: Conclusion.

In conclusion, the exploration of TM/graphene systems leads to several important observations. At low coverage, the doping efficiency is found to be related to the TM WFs, but Ti, Fe, and Pt all exhibit *n-type* doping even for materials with higher WF than graphene (i.e. Fe, Pt). Extending the Pt doping study to higher thickness, the doping can either be *n-type* or weakly *p-type*. Because WF considerations alone would generate strong *p-type* doping, this result provides experimental evidence for the strong interfacial dipole favoring *n-type* doping as predicted by theory [63]. Analysis of the scattering at low coverage indicates that the scattering by TM clusters exhibits different behavior compared to $1/r$ Coulomb scattering.

Chapter 4: Spintronic properties of graphene.

4.1: Introduction.

Graphene is an attractive material for spintronics [84] due to the observation of gate-tunable spin transport at room temperature [36, 85, 86] and the potential for long spin lifetimes (μs regime) arising from low intrinsic spin-orbit and hyperfine couplings [41, 87-89]. The extreme surface sensitivity of graphene [18] introduces the possibility of manipulating the spin transport properties by surface chemical doping. Furthermore, this enables new methods for investigating fundamental questions such as the origin of spin relaxation in graphene, which has become a central issue since experiments have realized spin lifetimes up to only a few hundred picoseconds [35, 42, 85, 89-94]. Recent experiments report that the primary source of spin relaxation is momentum scattering [91]. Furthermore, the dominant source of momentum scattering is believed to be charged impurity (CI) scattering[21, 95, 96]. Therefore, it is expected that CI scattering is an important factor for spin relaxation. In this thesis we investigate, for the first time, the effects of surface chemical doping on spin transport in graphene. Specifically, non-local spin signals of single-layer graphene spin valves are monitored *in situ* as gold adsorbates are deposited in ultrahigh vacuum and at cryogenic temperatures, and several important results are obtained. First, we demonstrate manipulation of the gate-dependent non-local spin signal as a function of sub-monolayer gold coverage. Second, we discover that CI scattering is not the dominant mechanism for spin relaxation, despite its importance for momentum scattering. Third, unexpected enhancements of the spin lifetime illustrate the

complex nature of spin relaxation in graphene and demonstrate the concept of spin-preserved chemical doping, which produces a three-fold enhancement of spin lifetime at fixed gate voltages. These results address both fundamental and applied issues that are important for the development of graphene spintronics.

4.2: Theory of spin transport in graphene. (Spin lifetime in graphene)

Spin life time in graphene is expected to be longer than 1 μs because of the low hyperfine interaction, namely the spin relaxation due to the coupling between electron spin and nuclear spin. This interaction is strongest when we have localized electrons. However, there are two aspects of graphene which may minimize the hyperfine interaction. First, graphene has free electrons which interact with nuclei weakly. Second, 99% of the carbon atoms in graphene are C_{12}, which has six protons and six neutrons and have no nuclear spin.

There are two mechanisms by which spin-orbit coupling could generate spin relaxation in graphene[97]. One is the Elliot-Yafet (EY) mechanism, in which a spin flip occurs with finite probability during a momentum scattering event, such as interactions with impurities, lattice defects, boundaries and phonons. The spin lifetimes will decrease with the decreasing of momentum scattering time, meaning $\tau_s \sim \tau_m$. The other is the Dyakonov-Perel (DP) mechanism, where spins experience an internal spin-orbit field $\vec{B}(\vec{k})$, which results in a precession with a Larmor frequency $\vec{\omega}(\vec{k}) = e/m\vec{B}(\vec{k})$. Because

the electrons (holes) that carry spins have different momenta, they will precess differently and pick up different phases. In contrast with the EY mechanism, where the spin relaxation happens at site of the collisions, in the DP mechanism, the spin relaxation happens in between the collisions. Therefore, in this case, spin relaxation is actually inversely proportional to the momentum scattering which means $\tau_s \sim \tau_m^{-1}$ [Figure 4.1].
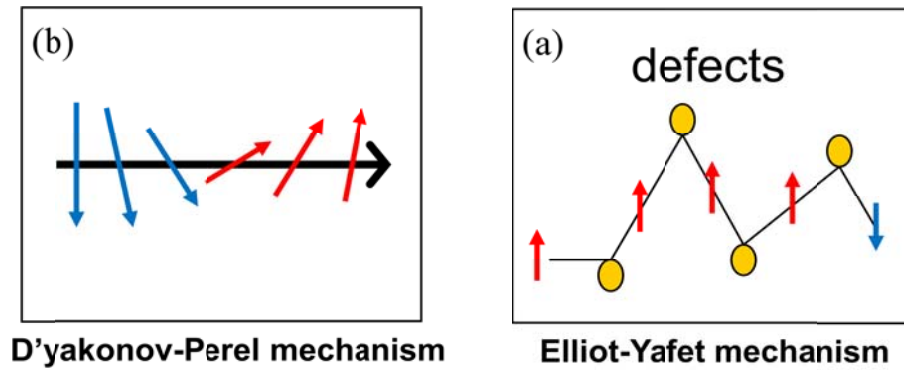
Figure 4.1 Schematic diagram of spin relaxation mechanisms for E-Y and D-P. (a) Elliot-Yafet mechanism - Spin flip during momentum scattering events. (b) D'yakonov-Perel mechanism - spins precess in internal spin-orbit fields.

The relationship between τ_s and τ_m, the momentum scattering time, is particularly important for understanding the spin relaxation. Recent work by van Wees shows that $\tau_s \sim D$ ($\sim \tau_m$) for graphene spin valves, indicating that the EY mechanism is more important than the DP mechanism.[91] However, their experiment was not directly varying the impurities or extrinsically adding extra momentum scattering on graphene. Instead, they

changed the carrier concentration in graphene and intrinsically increased the momentum scattering.

Therefore, to investigate the role of CI scattering on spin relaxation, our approach is to systematically introduce additional sources of CI scattering and monitor their effect on spin lifetime. Gold impurities are selected for this purpose because they have been shown to behave as CI scatterers with $1/r$ Coulomb potential[77] and are not expected to generate other effects such as resonant scattering, wavefunction hybridization, or chemical bonding [61, 98, 99].

It is expected that CI scattering will generate spin relaxation, based on theoretical calculations. As the TMs dope the graphene, charges transfer between TM and graphene. Therefore, it creates a magnetic field perpendicular to graphene and lifts the inversion symmetry. Group theory will allow an additional Bychkov-Rashba term and induce an extra spin relaxation [Ertler's paper]. The question is how this spin relaxation rate ($1/\tau_{CI}$) compares with the rates of other possible mechanisms (e.g. local lattice deformation,[42] substrate phonons,[94] etc.). If the various spin relaxation mechanisms are uncorrelated, then the total spin lifetime, τ_s, is given by $1/\tau_s = 1/\tau_{CI} + \sum_j 1/\tau_j$, where the summation is

over the other possible spin relaxation mechanisms. If CI scattering is the dominant spin relaxation rate, then $1/\tau_s \approx 1/\tau_{CI}$ and an increase in the amount of CI scattering will increase the overall spin relaxation rate. On the other hand, if another mechanism provides the dominant spin relaxation rate, then any changes to $1/\tau_{CI}$ will have negligible effect on the overall spin relaxation rate. Therefore, this study allows us to answer the

critical question: Is charged impurity scattering important for spin relaxation in graphene?

4.3: Device preparation (ebeam lithography and electrode pattern and MgO masking layer).

Figure 4.2a and b are the optical image and SEM image of the graphene spin valve non-local measurement geometry. The differences between the spin valve devices and Hall bar devices are electrode pattern, electrode material and device cleaning procedure. For spin valve devices, we evaporated 2 nm MgO masking layer at 7^0 away from normal, followed by 80 nm Co deposited at 0^0 away from normal [Figure 4.2c and d] [86, 90]. In this way, we are able to reduce the contact area and enhance the spin signal [100] [101]. Co is selected because it is a high-T_c FM material with T_c= 1388K which is much higher than room temperature. Electrodes are patterned all the way across the graphene layer and have the end extended away from the graphene edge by at least 2 μm to avoid effects from the stray fields. We caped the whole device with 5nm of Al_2O_3, deposited at 8^0 from normal, on top of Co to protect the edge of the electrodes from further oxidation. After the lift-off process, we load the sample directly into the UHV chamber without Hydrogen annealing in the tube furnace. This is because Co electrodes and MgO masking layer can be easily destroyed by Hydrogen. UHV annealing at 90^0 C was performed inside the UHV chamber to have a cleaner starting point.

(a) SLG, Co — Optical Microscope

(b) SLG, 500 nm — SEM image

(c) Co (7°), MgO (0°), SLG, SiO₂

(d) Co, MgO 2nm, SLG, SiO₂
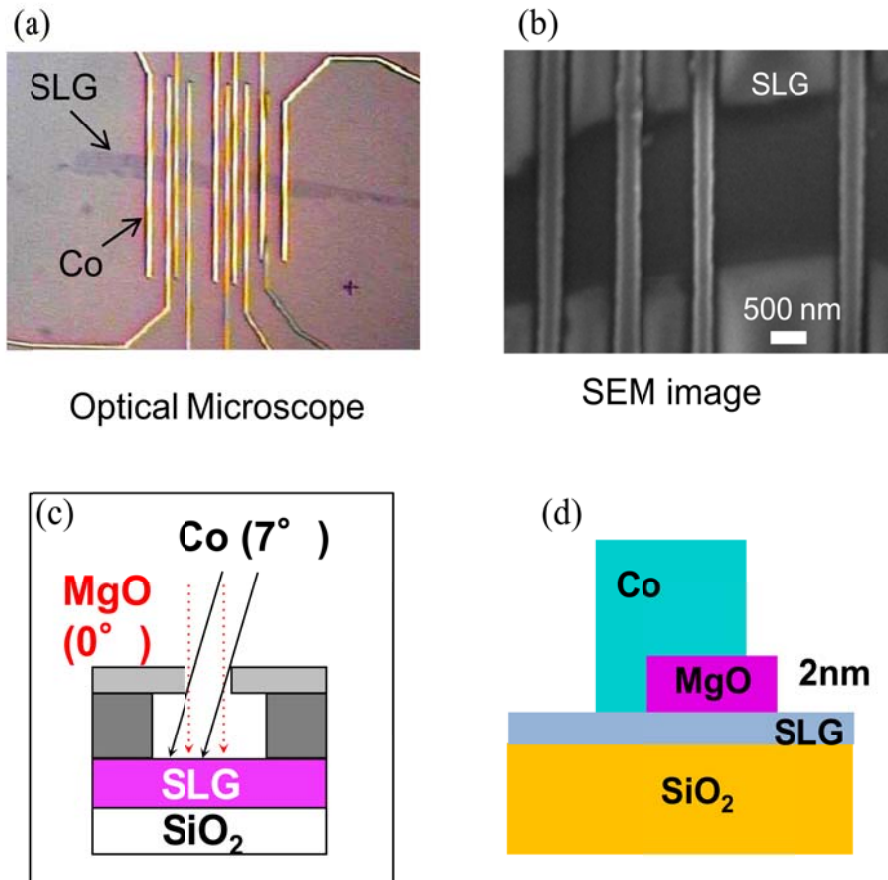
Figure 4.2 (a). Optical microscope image for spin valve device. (b). SEM image for spin valve device. (c). Schematic diagram of angle evaporation for MgO and Co. (d). Schematic drawing of completed device with Co in transparent contact and MgO as masking layer.

4.4: Result.

      4.4.1: Basic graphene spin valve characteristic.

Spin transport measurements are performed inside a molecular beam epitaxy (MBE) chamber with a base pressure of 1×10^{-10} torr. During the entire measurement, the sample is kept at low temperature (18 K) inside the chamber. We first measure the gate dependent conductivity on our spin valve device [Figure 4.3a]. The device shows a little electron-hole asymmetry and lower mobility compared to Hall bar devices. Without Hydrogen cleaning, these features are unavoidable due to resist residue from lithography step.

For the non-local measurement, we apply a current (I) across electrodes E2 and E1 while measuring the voltage (V) between electrodes E3 and E4. When spin transport is present, the non-local resistance ($R_{nl} = V/I$) is positive for parallel alignment and negative for antiparallel alignment of the E2 and E3 magnetizations. Figure 4.3b-d shows non-local magnetoresistance for a device with electrode spacing (E2 to E3) of $L = 2.5$ μm and the gate voltage (V_g) tuned to the hole transport regime ($V_D = -55$ V), charge neutrality point ($V_D = -15$ V) and the electron transport regime ($V_D = 25$ V). The spin signal, ΔR_{nl}, is defined by the difference between the parallel and antiparallel states, and has a value of 950 mΩ, 580 mΩ and 1100 mΩ, respectively.

Figure 4.3 (a). Gate dependent conductivity for spin valve device. (b). non-local spin signal at V_g= -55V. (c). non-local spin signal at V_g= -15V. (d). non-local spin signal at V_g= 25V.
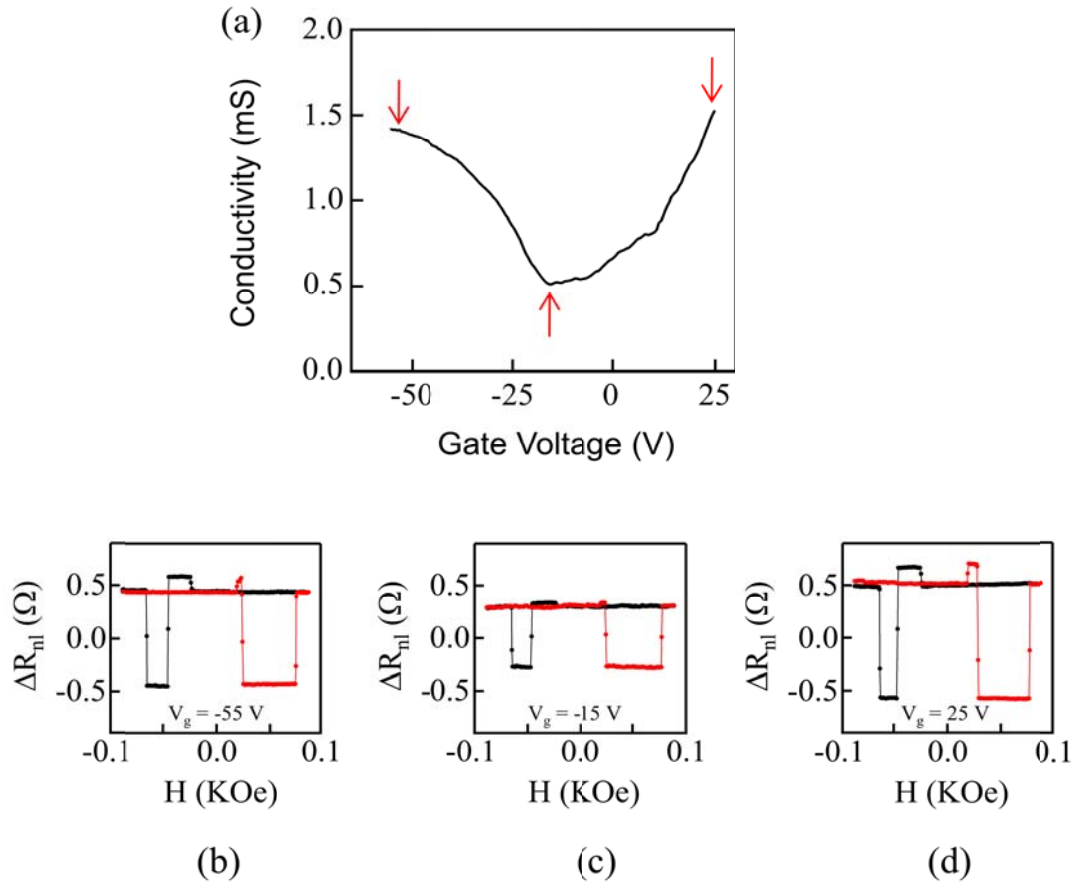
4.4.2: Gate dependent conductivity and gate dependent ΔR_{nl}.

We examine the effect of Au doping on charge transport properties by employing *in situ* transport measurements combined with MBE growth in ultrahigh vacuum. The Au is deposited from a thermal effusion cell with a growth rate of 0.04 Å/min while samples are maintained at 18 K to reduce the surface diffusion of the Au atoms[77]. Reference 81 shows the experimental evidence of Au acting as point like scatterers when we perform the growth at low temperature. For typical deposition times (less than 10 s total), the amount of Au is less than one percent of a monolayer. Figure 4.4a shows the gate-dependent conductivity (σ) for different amounts of Au coverage indicated by the deposition time (0 s, 2 s, 4 s, 6 s, 8 s) on a spin valve device. With increasing coverage, the Dirac point shifts toward negative gate voltage, which indicates that Au donates electrons to the graphene and the Au impurities become positively charged. Electron and hole mobilities are obtained by measuring the slope of the conductivity curve away from the Dirac point. Figure 4.5a shows that mobilities for electrons and holes decrease as a function of Au coverage. Despite the small amount of Au deposited, the mobility diminishes by more than half. This indicates that the CI scattering introduced by Au impurities exceeds the scattering initially present in the clean device.

We next consider the effect of the Au doping on the spin transport properties. A model for lateral spin transport was developed by Takahashi *et. al.*[100], and we apply the same method to obtain an expression for the non-local spin signal of graphene spin valves with transparent contacts:
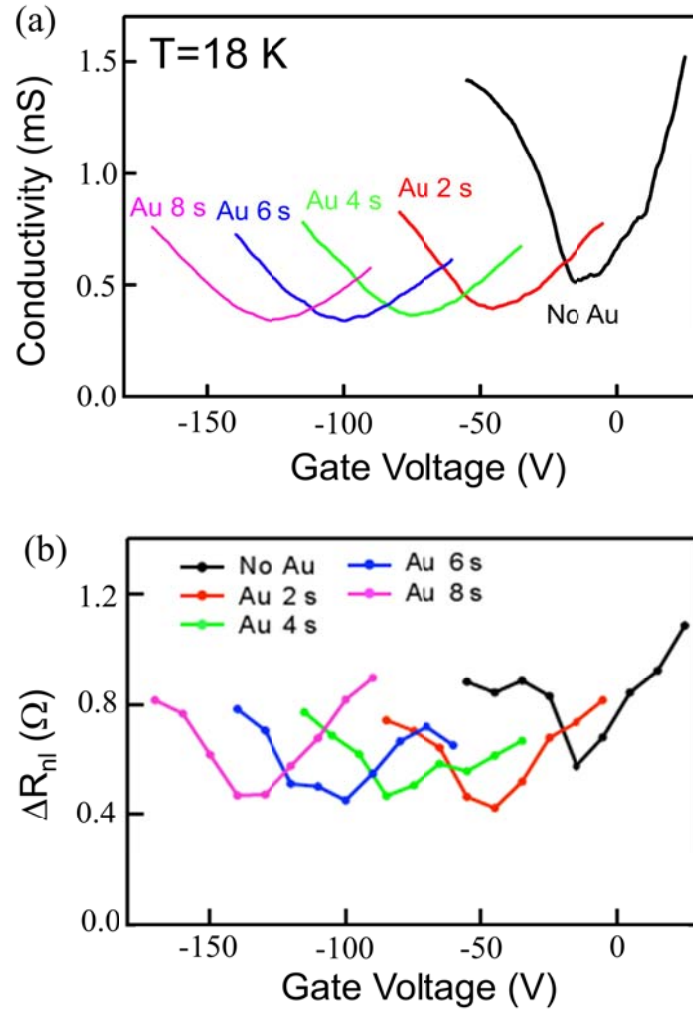
Figure 4.4 (a). Gate dependent conductivity for different amounts of Au doping (0 sec, 2 sec, 4 sec, 6 sec and 8 sec). (b). Gate dependent DR$_{NL}$ for different amounts of Au doping (0 sec, 2 sec, 4 sec, 6 sec and 8 sec).

$$\Delta R_{nl} = C\sigma f(\lambda_s), \quad C = \frac{4P_F^2}{\left(1-P_F^2\right)^2} \frac{\rho_F^2 \lambda_F^2}{A_J^2} \frac{W}{L} \ , \quad f(\lambda_s) = \frac{L}{\lambda_s}\left[\frac{\exp(-L/\lambda_s)}{1-\exp(-2L/\lambda_s)}\right] \quad (4.1)$$

where L is the electrode spacing, W is the graphene width, λ_s is the spin diffusion length of graphene, P_F is the spin polarization of the ferromagnet, and ρ_F is the resistivity of the ferromagnet, λ_F is the spin diffusion length of the ferromagnet, and A_J is the area of the junction between the ferromagnet and graphene. The prefactor, C, consists of terms that are not altered by Au doping, and therefore we can treat this as a constant factor for all ΔR_{nl} data. Doping can affect ΔR_{nl} either through changes in the spin diffusion length or the (spin independent) conductivity. Figure 4.4b shows the gate dependence of the non-local magnetoresistance for different Au coverages (0 s, 2 s, 4 s, 6 s, 8 s). In agreement with equation (1), ΔR_{nl} tracks the gate dependence of the conductivity, with minimum values of the ΔR_{nl} curves coinciding with the Dirac point. Furthermore, the overall magnitude of ΔR_{nl} remains relatively unchanged, which indicates that the Au atoms do not dramatically suppress the spin diffusion length. This demonstrates that the manipulation of the non-local spin signal is mostly attributed to the effect of Au doping on the conductivity.

To quantify the effect that Au doping does have on the spin diffusion length, we consider the ratio $\Delta R_{nl}/\sigma$. Referring to equation (1), this ratio factors out the strong effect that the Au doping has on the conductivity, thus leaving only the part that depends on the spin diffusion length [$\Delta R_{nl}/\sigma = C f(\lambda_s)$]. Because f is a monotonic function of λ_s (see Figure 4.5b, with $L = 2.5$ μm), an increase (decrease) in $\Delta R_{nl}/\sigma$ corresponds to an

increase (decrease) in λ_s. At typical values of λ_s between 1 and 3 μm, the value of f varies significantly. For each Au coverage, we average the value of $\Delta R_{nl}/\sigma$ over gate voltages within $\pm$35 V of the Dirac point. As shown in Figure 4.5c, $\langle \Delta R_{nl}/\sigma \rangle$ does not decrease with Au coverage, which implies that the average λ_s does not decrease with Au coverage. This behavior shows that CI scattering is not important for spin relaxation in graphene. An unexpected trend is that $\langle \Delta R_{nl}/\sigma \rangle$, and hence λ_s, actually increases slightly with Au coverage. This suggests that the Au impurities produce a slight suppression of the spin relaxation. □
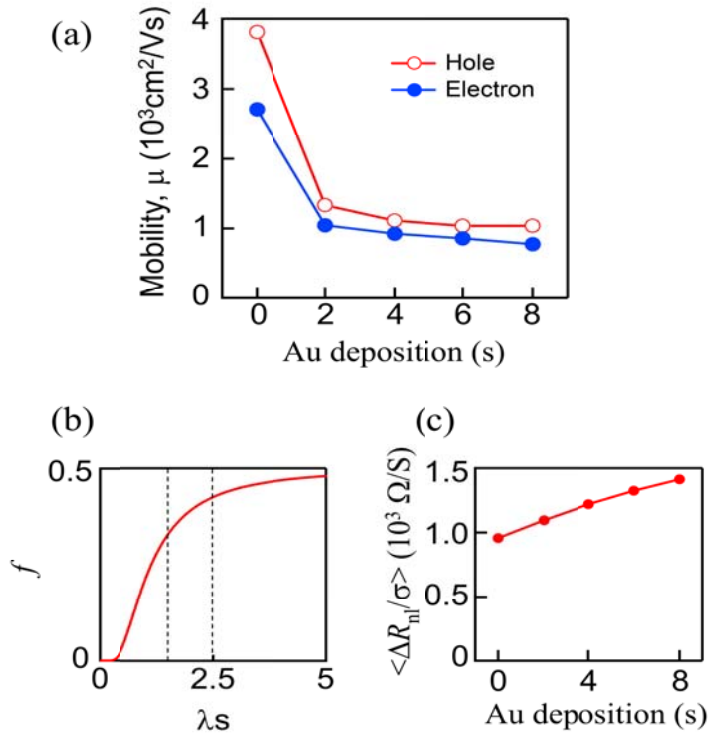
Figure 4.5 (a). Mobilities for electrons and holes at different amounts of Au doping. (b). f-function for different l_s. The two dashed lines indicate where l_s=1.5 mm and l_s=2.5 mm respectively. (c). Plot modified DR$_{nl}$ (<DR_{nl}/s>) vs. Au deposition.

4.4.3: Hanle procession measurement.

The role of CI scattering on spin relaxation is investigated further with a different type of experiment. We directly measure τ_s by applying an out-of-plane magnetic field to induce electron spin precession (Hanle effect, figure 4.6) [85, 90].
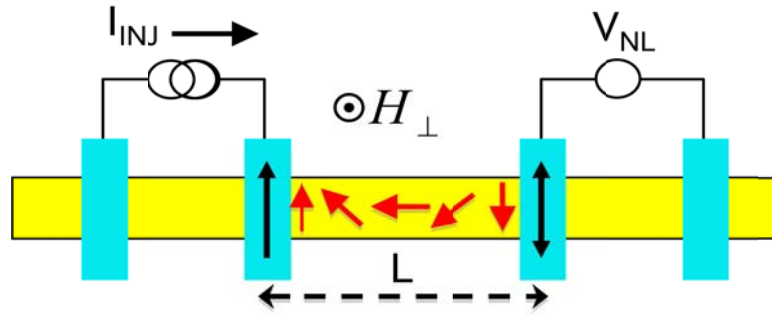
Figure 4.6 Schematic diagram of Hanle measurement on spin device.

Figures 4.7a-f show the representative Hanle data and best fit curves for different amounts of Au coverage (0 s and 8 s). The top (bottom) curve is for the parallel (antiparallel) alignment of the E2 and E3 magnetizations. For the fitting, we first obtain the symmetric part of the data, $[R_{nl}(H)+R_{nl}(-H)]/2$, to remove effects unrelated to spin. A constant background is subtracted and the parallel and antiparallel data are simultaneously fit with the following equation using the same values for τ_s and D, but different values for the amplitude S_0:

$$R_{nl}^{P(AP)} = (\pm)S_0 \int \frac{1}{\sqrt{4\pi Dt}} \exp\left[-\frac{L^2}{4Dt}\right] \cos(g\mu_B H_\perp / \hbar) \exp(-t/\tau_s) dt$$

(4.2)

where g is the g-factor, μ_B is the Bohr magneton, $H_\perp$ is the out-of-plane magnetic field, electrode spacing L is 2.5 µm, and the + (-) sign is for the parallel (antiparallel) magnetization state.
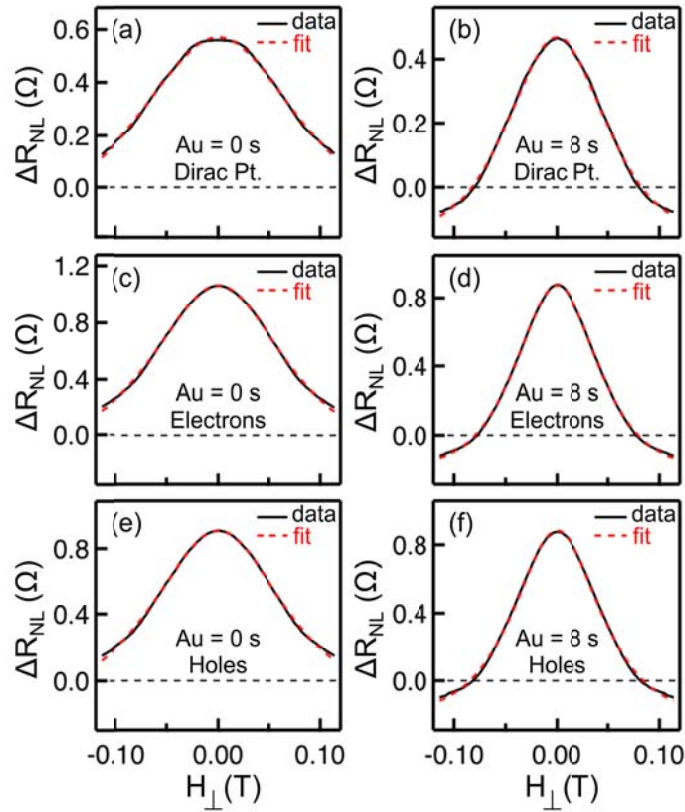
Figure 4.7 Hanle curves for 0 sec and 8 sec of gold deposition at electron transport (c,d), hole transport (e,f) and charge neutrality point (a,b).

4.4.4: Spin lifetime and Spin diffusion constant.

Figure 4.8a and b show the best fit values of D and τ_s as a function of Au coverage at the Dirac point (black squares), for an electron concentration of 2.9×10^{12} cm^{-2} (red circles), and for a hole concentration of 2.9×10^{12} cm^{-2} (blue triangles). The error bars shown on the figure was obtained by curve fitting within 99% of the confidence level. This confidence level included the standard deviation and the uncertainties of best fit by changing multiple parameters at the same time. In all three cases, D decreases as function of Au coverage, which is expected since we added extra scatters onto graphene. The behavior of D follows the trend observed in the sample mobility, as shown in figure 4.5a, where D also decreases with increasing Au coverage and gradually saturates at higher coverage. For τ_s, all three cases show a slight enhancement with increasing Au coverage. This result is in good agreement with previous assumption in 4.4.2, which demonstrated that, charged impurities are not the dominant spin relaxation mechanism in graphene.

However, this enhancement of τ_s can't be explained by simply saying that charged impurities are not the dominant spin relaxation mechanism. The presence of Au must be suppressing other types of relaxation mechanisms. As we mentioned in section 4.2, the signature behavior for EY mechanism is $\tau_s \sim \tau_m$, whereas for DP mechanism $\tau_s \sim \tau_m^{-1}$. In figure 4.8a and b we observe that D decreases with Au coverage while τ_s exhibits a slight increase, illustrating that the $\tau_s \sim D$ ($\tau_s \sim \tau_m$) scaling is not obeyed. This does not necessarily argue against EY, but rather points out that many different types of

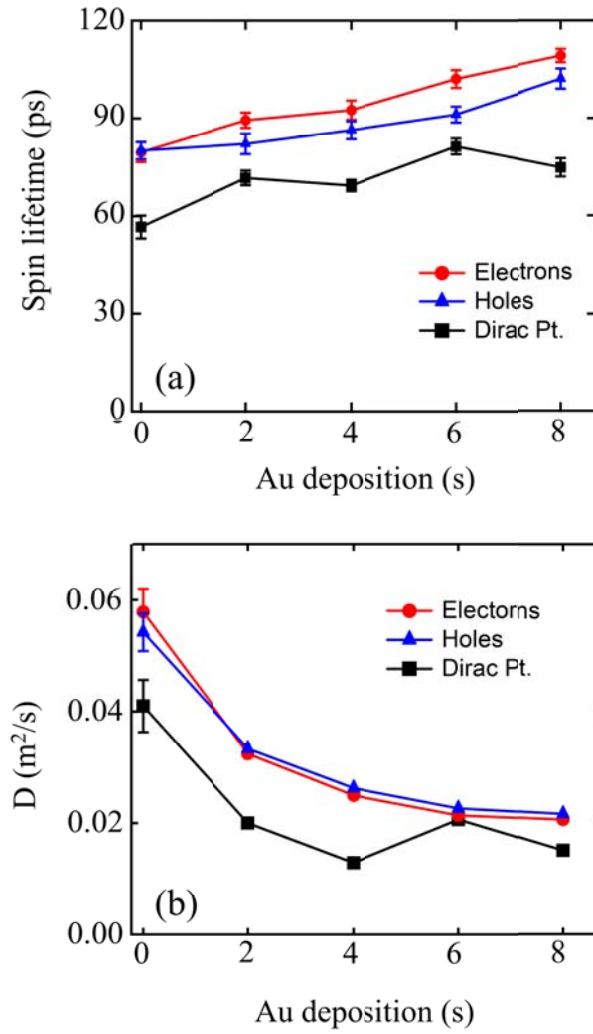Figure 4.8 (a). Spin lifetime vs. Au coverage for electron transport (Red), hole transport (Blue) and charge neutrality point (Black). (b). Diffusion constant vs. Au coverage for electron transport (Red), hole transport (Blue) and charge neutrality point (Black).

momentum scattering can produce EY spin relaxation (i.e. CI scattering, phonons, local sp^3 deformation, edge scattering, short-range impurity potential, etc.) [42, 93, 94], and each type of momentum scattering can have a different efficiency for spin scattering. Stated in another way, if the dominant momentum scattering mechanism is different from the dominant EY spin relaxation mechanism, then τ_m and τ_s need not show any particular relation. Our results indicate that CI scattering is very effective for momentum scattering, but it produces negligible spin relaxation on the time scale of ~100 ps.

There are several possible effects which may result in the slight increase of τ_s with Au coverage. The first possibility is that the spin relaxation mechanisms are correlated. For uncorrelated mechanisms, the spin relaxation rates simply add (as discussed earlier) so that any additional relaxation cannot increase the overall spin lifetime. In our case, a correlation might arise if the gold impurities actively inhibit some of the other spin relaxation mechanisms. For instance, the gold may bind to lattice defects or edge sites [102, 103], reducing their ability to scatter spins. A second possibility is that DP makes a non-negligible contribution to the overall spin relaxation. While the scaling of τ_s with D observed by van Wees [91] favors the EY-type mechanisms and the intrinsic DP mechanism should be very weak due to the low intrinsic spin-orbit coupling [41, 87, 88], some theoretical calculations suggest that a curvature-enhanced DP mechanism could contribute to the overall spin lifetime [41]. If DP provides an appreciable contribution, then the slight enhancement could occur because $\tau_S^{DP} \sim \tau_m^{-1}$. The unanticipated increase of τ_s highlights the complex nature of spin relaxation in graphene and motivates further

systematic studies of its origin.

4.4.5: Enhanced spin properties with chemical doping.

The robustness of spin polarization against CI scattering may prove to be useful for future applications. In principle, impurities could be used to tune the carrier concentration without inducing additional spin relaxation. To demonstrate this idea, we investigate ΔR_{nl} and σ as a function of Au doping at fixed gate voltage (V_g = -15 V, the initial Dirac point). As shown in Figure 4.10a, σ increases as a result of the substantial increase in carrier concentration, and ΔR_{nl} follows the trend due to the linear scaling with σ (equation 1). Figure 4.10b shows a significant enhancement in the spin lifetime, τ_s, from 50 ps to 150 ps at the highest Au coverage. This is a fortuitous situation where τ_s increases due to the higher carrier concentration [91] combined with the lack of additional spin relaxation. This demonstrates the concept of spin-preserved chemical doping of carriers, which provides a potentially useful tool in the design of future graphene spintronic devices.
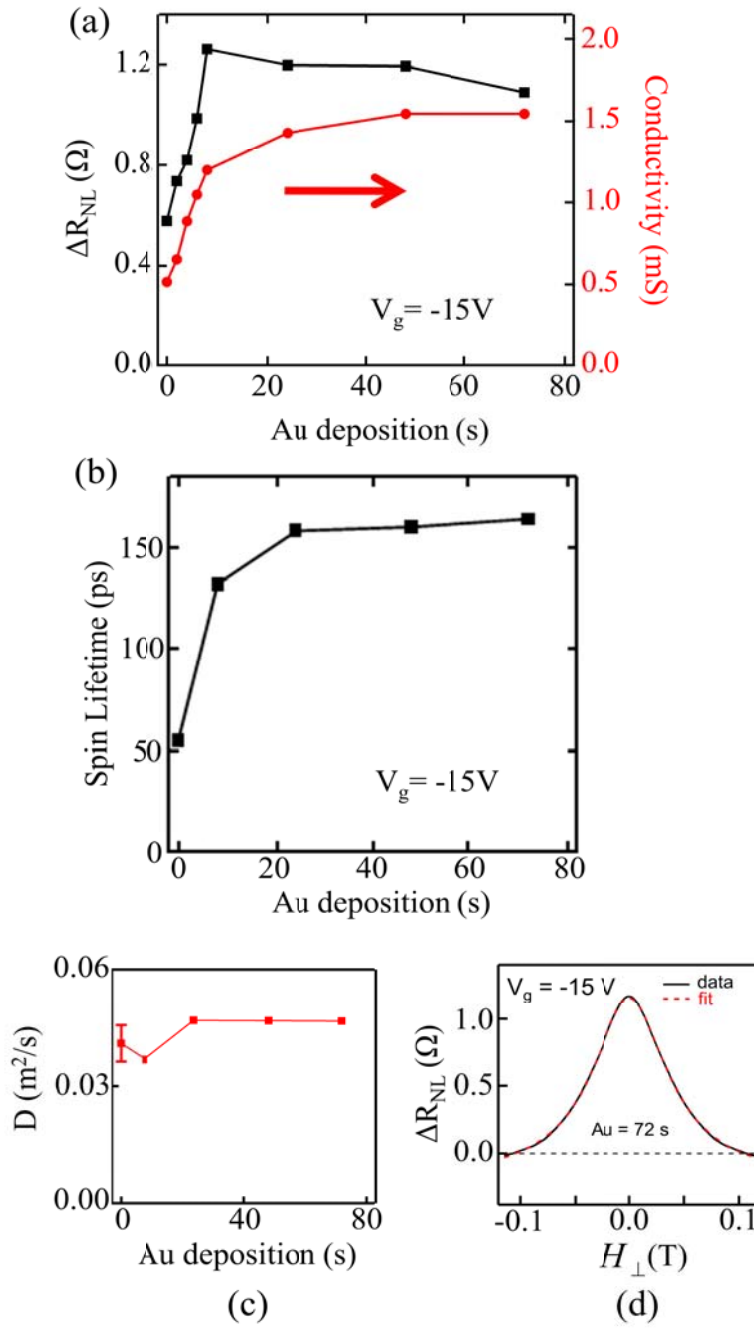
Figure 4.9 High coverage (up to 72 sec) data: (a). Au coverage vs. conductivity (Red curve) and Au coverage vs. ΔR_{nl} (black curve) with back gate voltage fixed at V= -15 V. (b). Spin lifetime vs. Au coverage. (c). Diffusion constant vs. Au coverage. (d). Hanle curve for 72 seconds of Au coverage.

4.5 Conclusion:

In conclusion, we have demonstrated the manipulation of spin transport properties in graphene through chemical doping. The results clearly show that CI scattering is not the primary source of spin relaxation in graphene, even though it is very effective at generating momentum scattering. Additionally, an enhancement of spin lifetime is observed with increased gold coverage, which may become useful for future graphene spintronic devices.

Chapter 5: Conclusion.

For the last six years of my graduate school career, I have been investigating the electronic properties and spintronic properties of doped graphene. By using a specially designed system, we realized that all three TMs, Ti, Fe, and Pt, introduced *n-type* doping to graphene, even though their bulk work functions are smaller, similar to, and larger than graphene. The observation of this phenomenon is the first experimental evidence of an interfacial dipole forming in between TMs and graphene. In additional to this, we also studied the scattering introduced by TM doped graphene and realized the dominant scattering mechanism resulting from Ti and Pt doping is charged impurity scattering. Experimental data show that even when the amount of Pt deposited is ten times larger than Ti, the normalized mobility vs. dirac point shift still follows the same fitting curve. This study also suggested some future studies, such as understanding the electron hole asymmetry due to the ferromagnetic adatoms/clusters. The special system used in this study can possibly be used to demonstrate other interesting physics ideas modeled by having TM adatoms on top of graphene[57, 58, 60, 62, 104].

For spin studies, we showed both non-local signal and spin lifetime do not decrease with increasing amounts of Au deposition. We demonstrated the most important charge scattering mechanism, Coulomb scattering, is not the dominant spin scattering mechanism in graphene with τ_s ~ 100 ps range. Recent studies show that one of the limiting factors of the measured spin lifetime in graphene is the Co-graphene interface [105]. By inserting an MgO tunnel barrier, spin lifetimes have been reported up to 500 ps.

However, even with this breakthrough, there is still a big gap between theoretically predicted spin lifetimes and experimentally observed spin lifetimes. There are many other effects that might be responsible for the short spin lifetimes, such as edge scattering, ripple induced magnetic fields, lattice distortions etc. Further studies are needed in order to better improve the spin transport characteristics.

Graphene is overall a strong candidate for future electronic and spintronic device applications due to its amazing properties. It shows the potential to be a key factor for the integration of logic devices and memory storage devices. I hope my studies in this field can help to develop the future technology.

Appendix A: Evaporator designed.

Ebeam evaporator:

This evaporator is designed to use high energy electron beam to locally heat up the target materials [106]. Other then the support structure, there are four major parts of the cell; Shell, filament, grid and target. Filament is made from a piece of tungsten wire. Tungsten wire is chosen because it increased the stability of the cell performance. After an annealing treatment, tungsten wire becomes rigid keeping the distance between grid and filament constant. Therefore, we can get the stable growth rate with similar applied filament current. The grid is made by a thin tantalum grid with two concentric support rings. Filament will start emitting electrons with applied current above 5 A. These electrons can be accelerated toward grid by applying 200 Volts (medium voltage) on the grid.

Before we apply high voltage (1kV to 5 kV) onto the target, we can read a big emission current from the grid. This is because most of the emitted electrons from the filament are drained through the grid. When we gradually turn on the target voltage, we observed the emission currents on the grid dcreases and the emission currents on the target increasing. This behavior indicates that most of the electrons accelerated towards the grid are actually pass through it. Without the target material at high voltage though, these electrons move back to the grid and increasing emission currents on the grid. However, once we have high voltage on the target, these electrons are attracted toward the target instead of the grid thus heating the material and causing it to evaporate.

The shell prevents the electrons from directly "seeing" the sides of the high voltage target. If the shell weren't in place, the electrons would heat up the target from all sides causing a failure in the cell. The shell allowing the electrons to only see the end of the target rod (at high voltage) after they pass through the grid allowing for a control material flux. The shell also provides a cover for grid and filament from being coated by the target material.
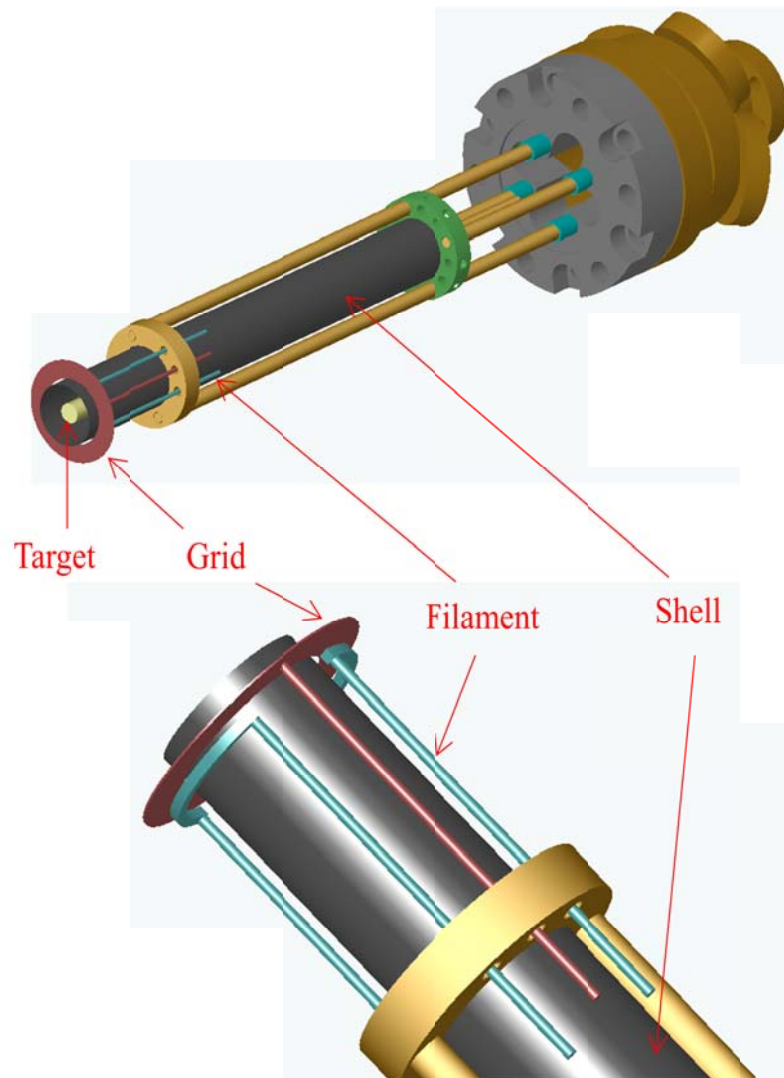
Figure A1. SolidWorks drawing for the ebeam cell with an overall view and a zoom-in view of the tip part.

Thermal evaporator:

Thermal effusion evaporator uses the principle of heating a metal to it evaporating temperature through a heater. We use a tungsten heater to heat up the crucible filled with the evaporate material. We usually use this kind of evaporator to deposit materials which have evaporation temperature lower than 1400 ^{0}C. There are four main parts of the cell; thermocouple, molybdenum support rods, tungsten heater and crucible. We use molybdenum support rods as positive and negative lead for current source and connect the tungsten wire with the rods. We can easily get above 1200 ^{0}C on the crucible with output power ~360W (30 V, 12A) by intensively wrapping the tungsten wire onto the crucible. The temperature is monitored through a type c or type k thermocouple wire contacting the bottom of the crucible. We use an Eurotherm temperature controller in combination with a Sorensen power supply for feedback control over the cell and control the temperature in precision of 0.1 ^{0}C.
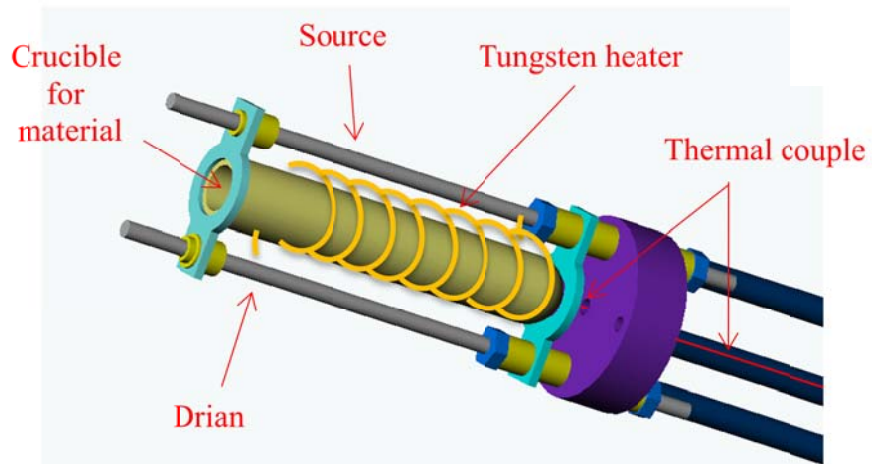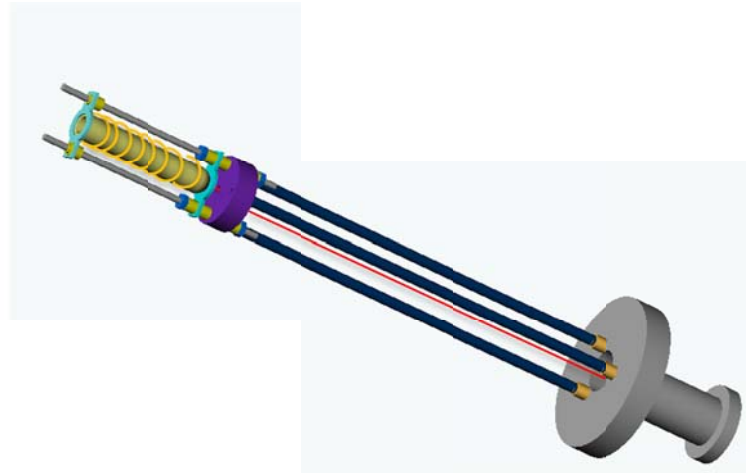
Appendix A2. SolidWorks drawing of thermal cell.

Appendix B: Current Source

This current box can convert voltage to current. This particular design provides two major advantages. First of all, we are able to tune the amplification ration by tuning the R_X. In my case, I have the current box with conversion factor of 1mA/μV. Second, regardless of the load resistance, the current output will stay constant.

Circuit drawing.
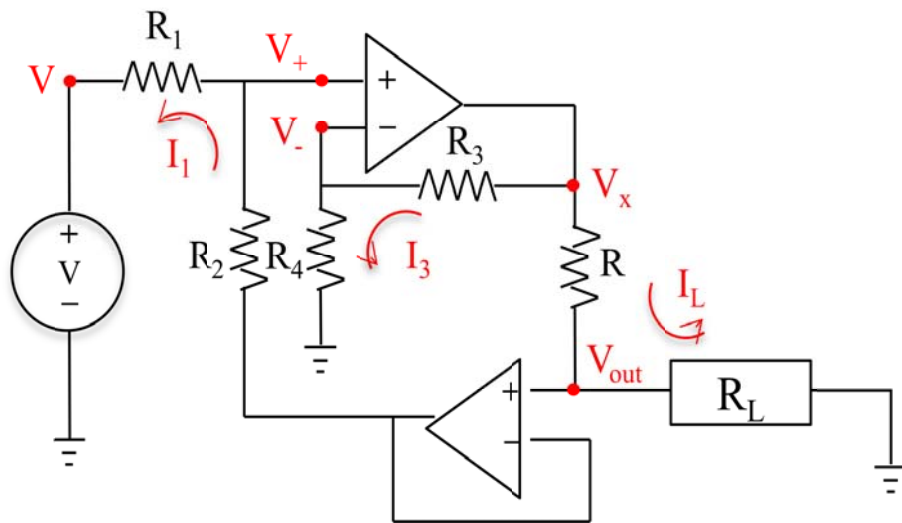
Figure B.1 Circuit for current source.

Circuit analysis.

$$\frac{V_+ - V}{R_1} = \frac{V_{out} - V_+}{R_2} \qquad \text{(B.1)}$$

$$\frac{V_x - V_+}{R_3} = \frac{V_+}{R_4} \qquad \text{(B.2)}$$

$$I_L = \frac{V_6 - V_{out}}{R} \qquad \text{(B.3)}$$

$$V_{out} = I_L R_{Load} \qquad \text{(B.4)}$$

After solving these four equations, we are able to get the relation between the load resistance (R_L) and the applied voltage (V) [equation B.5].

$$\frac{R_2}{R_1} V = \frac{\left(\frac{R_2}{R_1} + 1\right)}{\left(\frac{R_3}{R_4} + 1\right)} R I_L + \frac{\left(\frac{R_2}{R_1} + 1\right)}{\left(\frac{R_3}{R_4} + 1\right)} R_L I_L + R_L I_L \qquad \text{(B.5)}$$

If we have designed the circuit to have $\frac{R_2}{R_1} = \frac{R_3}{R_4}$, equation B.5 can be simplified to

$$I_L = \frac{V}{R}.$$

Therefore, we can have a stable output current source which won't change with the load resistance.

Appendix C: Derivation for nonlocal spin signal [100].
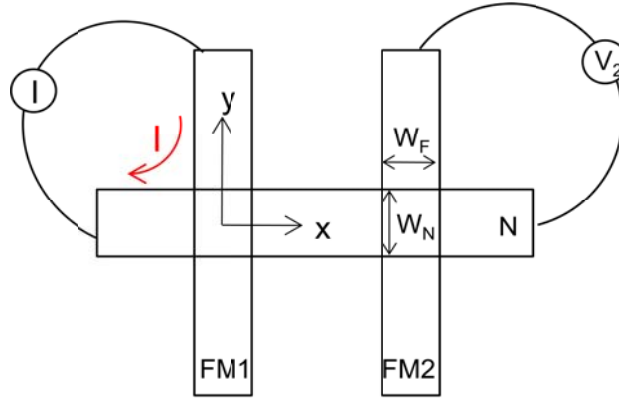
Figure C.1. Nonlocal device.

Equation 1 is the electrical current for different spin channel σ driven by the electric field E.

$$j_\sigma = \sigma_\sigma E - eD_\sigma \nabla(\delta n_\sigma)$$ ……………………………………….. (1)

By considering the diffusive case for spin transport and using the Einstein relation in equation (2).

$$\delta n_\sigma = N_\sigma \delta \varepsilon_\sigma \quad , \quad \sigma_\sigma = e^2 N_\sigma D_\sigma$$ ………………………………. (2)

We can have our first important equation: the relation between spin current and spin dependent chemical potential [equation a].

$$j_\sigma = -(\sigma_N/e)\nabla(\delta\mu_N)$$ …………………………………………...........................(a)

The continuity equation for charge and spin in the steady state are $\nabla(j^\uparrow + j^\downarrow) = 0$ and

$\nabla(j^\uparrow - j^\downarrow) = -e\delta n_\uparrow/\tau_{\uparrow\downarrow} + e\delta n_\downarrow/\tau_{\downarrow\uparrow}$, where $\tau_{\sigma\sigma'}$ is the scattering time between two spin

states. Using the relation $N_\uparrow/\tau_{\uparrow\downarrow} = N_\downarrow/\tau_{\downarrow\uparrow}$ we can get equation (b)

$$\nabla^2(\sigma_\uparrow\mu_\uparrow + \sigma_\downarrow\mu_\downarrow) = 0 \quad \text{and} \quad \nabla^2(\mu_\uparrow - \mu_\downarrow) = \lambda^{-2}(\mu_\uparrow - \mu_\downarrow)$$ …………………….…. (b)

We now consider the electrical current and spin current at FM1/NM interface and FM2/NM interface. We first write down the chemical potential in the NM.

To satisfy equation b, we can have chemical potential in non-magnetic metal (NM) (spin transport layer) as:

$$\mu_N^\sigma(x) = \overline{\mu_N} + \sigma\delta\mu_N \quad , \quad \overline{\mu_N} = 0 \quad \text{for} \quad x>0, \quad \overline{\mu_N} = (\frac{eI}{\sigma_N})x \quad \text{for} \quad x<0 \quad \text{and}$$

$$\delta\mu_N = a_1 e^{-|x|/\lambda_N} + a_2 e^{-|x-L|/\lambda_N}.$$

Using equation (a) and $j_i^s = j_i^\uparrow - j_i^\downarrow$, we can calculate the spin current inside the NM at the interface of FM1 and FM2 (i=1, 2) as equation (c).

$$I_i^s = 2(\frac{\sigma_N A_N}{e\lambda_N})a_i$$

.... (c)

As in the NM, we can also set the chemical potential in FM (spin injector and spin

detector) as $\quad \mu_F^\sigma(z) = \overline{\mu_F} + \sigma b_i (\sigma_F / \sigma_F^\sigma) e^{-z/\lambda_F}$, where $\overline{\mu_F} = (\frac{eI}{\sigma_F A_J})z + eV_1$ inside FM1

and $\overline{\mu_F} = eV_2$ inside FM2, and calculate the spin current without considering the spin flip

at the interface. We can get the spin current for FM1 and FM2 as:

$$I_1^s = P_F I - 2(\frac{\sigma_F A_J}{e\lambda_F})b_1$$

.... (d)

$$I_2^s = -2(\frac{\sigma_F AJ}{e\lambda_F})b_2$$

.... (e)

We also consider the spin current at the interface by using Ohm's law and considering

the voltage drop across the interface: $I_i^\sigma = (\frac{G_i^\sigma}{e})(\mu_F^\sigma\big|_{z=0^+} - \mu_N^\sigma\big|_{z=0^-})$, where

$G_i = G_i^\uparrow + G_i^\downarrow = R_i^{-1}$. By using the expression of μ_F^σ and μ_N^σ, we can get :

$$I_1^s = P_J V_1 - \frac{a_1}{e} - \frac{a_2}{e}e^{-L/\lambda_N} + (\frac{G_1^\uparrow}{\sigma_F^\uparrow} + \frac{G_1^\downarrow}{\sigma_F^\downarrow})R_1 \frac{\sigma_F}{e}b_1$$

.... (f)

$$I_2^s = P_J V_2 - \frac{a_2}{e} - \frac{a_1}{e}e^{-L/\lambda_N} + (\frac{G_2^\uparrow}{\sigma_F^\uparrow} + \frac{G_2^\downarrow}{\sigma_F^\downarrow})R_i \frac{\sigma_F}{e}b_2$$

.... (g)

To match the boundary condition, we need to have the spin current in FM1, the interface and the NM match each other. Therefore, we can have four equations by combining eq. (c)-(g).

For spin current conservation:

At FM_1:

$$I_1^s = 2\frac{R_1}{R_N}a_1 = P_F IeR_1 - 2\frac{R_1}{R_F}b_1 = P_J V_1 - \frac{a_1}{e} - \frac{a_2}{e}e^{-L/\lambda_N} + (\frac{G_1^\uparrow}{\sigma_F^\uparrow} + \frac{G_1^\downarrow}{\sigma_F^\downarrow})R_1\frac{\sigma_F}{e}b_1 \quad \text{... (h)}$$

At FM_2:

$$I_2^s = 2\frac{R_2}{R_N}a_2 = 2\frac{R_2}{R_F}b_2 = P_J V_2 - \frac{a_2}{e} - \frac{a_1}{e}e^{-L/\lambda_N} + (\frac{G_2^\uparrow}{\sigma_F^\uparrow} + \frac{G_2^\downarrow}{\sigma_F^\downarrow})R_i\frac{\sigma_F}{e}b_2 \quad \text{...............(i)}$$

We also need to have the electrical current conserved at the interface, meaning $I_i = I_i^\uparrow + I_i^\downarrow$ also have to satisfy the boundary condition. Considering we only have current flowing through FM1 and have no current flowing through the FM2, we can have two equations:

At FM_1 (Where all the current passes through):

$$IR_1 = V_1 - P_J \frac{a_1}{e} - P_J \frac{a_2}{e} e^{-L/\lambda_N} + (\frac{G_1^\uparrow}{\sigma_F^\uparrow} - \frac{G_1^\downarrow}{\sigma_F^\downarrow})R_1 \frac{\sigma_F}{e} b_1$$

...............................(j)

At FM$_1$ (Where there is no current):

$$o = V_2 - P_J \frac{a_2}{e} - P_J \frac{a_1}{e} e^{-L/\lambda_N} + (\frac{G_2^\uparrow}{\sigma_F^\uparrow} - \frac{G_2^\downarrow}{\sigma_F^\downarrow})R_2 \frac{\sigma_F}{e} b_2$$

...............................(k)

Now we have six equations (h, i, j, k) and six unknown (V$_1$, V$_2$, a$_1$, a$_2$, b$_1$, b$_2$). To make the algebra easier we let

$$G_i^\uparrow = \frac{1}{2}\frac{1+P_J}{R_i}, G_i^\downarrow = \frac{1}{2}\frac{1-P_J}{R_i}, \sigma_F^\uparrow = \frac{1}{2}\sigma_F(1+P_F), \sigma_F^\downarrow = \frac{1}{2}\sigma_F(1-P_F)$$

and rewrite these six equations:

$$IR_1 = V_1 - P_J \frac{a_1}{e} - P_J \frac{a_2}{e} e^{-L/\lambda_N} + (\frac{1+P_J}{1+P_F} - \frac{1-P_J}{1-P_F})\frac{1}{e} b_1$$

$$o = V_2 - P_J \frac{a_2}{e} - P_J \frac{a_1}{e} e^{-L/\lambda_N} + (\frac{1+P_J}{1+P_F} - \frac{1-P_J}{1-P_F})\frac{1}{e} b_2$$

$$b_1 = \frac{1}{2}P_F IeR_F - \frac{R_F}{R_N}a_1$$

$$b_2 = -2\frac{R_F}{R_N}a_2$$

79

$$P_J V_2 - \frac{a_2}{e} - \frac{a_1}{e} e^{-L/\lambda_N} + \left(\frac{1+P_J}{1+P_F} + \frac{1-P_J}{1-P_F}\right)\frac{1}{e} b_2 = 2\frac{R_2}{R_N} a_2$$

$$P_J V_1 - \frac{a_1}{e} - \frac{a_2}{e} e^{-L/\lambda_N} + \left(\frac{1+P_J}{1+P_F} + \frac{1-P_J}{1-P_F}\right)\frac{1}{e} b_1 = 2\frac{R_1}{R_N} a_1$$

After working out the algebra, we can get the coefficient a_1 and a_2.

$$a_1 = \frac{-a_2}{(1-P_J^2)e^{-L/\lambda_N}}\left[\frac{2(1-P_J^2)}{1-P_F^2}\frac{R_F}{R_N} + (1-P_J^2) + 2\frac{R_2}{R_N}\right]$$

$$a_2 = R_N e^{-L/\lambda_N}\left(\frac{eP_F R_F}{1-P_J^2} + \frac{eP_J R_1}{1-P_F^2}\right) \times \left(\prod_{i=1}^{2}\left(1+\frac{2\frac{R_i}{R_G}}{1-P_J^2} + \frac{2\frac{R_F}{R_G}}{1-P_F^2}\right)^2 - e^{-2L/\lambda_G}\right)^{-1}$$

The nonlocal resistance is defined as the voltage created by the spin chemical potential

different at FM2 interface divided by the injection current.

$$R_{NL} = \frac{V_2}{I} = 2R_N e^{-L/\lambda_N}\prod_{i=1}^{2}\left(\frac{P_J\frac{R_i}{R_G}}{1-P_J^2} + \frac{P_F\frac{R_F}{R_G}}{1-P_F^2}\right)^2 \times \left(\prod_{i=1}^{2}\left(1+\frac{2\frac{R_i}{R_G}}{1-P_J^2} + \frac{2\frac{R_F}{R_G}}{1-P_F^2}\right)^2 - e^{-2L/\lambda_G}\right)^{-1}$$

Appendix D: Tight binding model for graphene band structure.

$$\psi_k = \sum_{n_i n_j} e^{i\vec{k}\vec{R}_j} \left[A\phi_A(\vec{r}_i - \vec{R}_j) + B\phi_B(\vec{r}_i - \vec{R}_j) \right] \qquad \vec{R}_j = n_i\vec{a}_1 + n_j\vec{a}_2$$

$$H|\psi_k\rangle = E|\psi_k\rangle \qquad H = \frac{p^2}{2m} + U(\vec{r})$$

Consider the nearest neighbors

For site A, we have ($n_i=0$, $n_j=1$), ($n_i=1$, $n_j=0$), ($n_i=0$, $n_j=0$).

$$|\psi_k\rangle = A|\phi_A\rangle + B|\phi_B\rangle + Be^{i\vec{k}\vec{a}_1}|\phi_B\rangle + Be^{i\vec{k}\vec{a}_2}|\phi_B\rangle$$

$$\langle \phi_A |H|\psi_k\rangle = \langle \phi_A |E|\psi_k\rangle$$

For

$$\langle \phi_A |\phi_A\rangle = 1, \langle \phi_A |\phi_B\rangle = 0$$

We have equation D.x become

$$A\langle \phi_A |H|\phi_A\rangle + B(1 + e^{i\vec{k}\vec{a}_1} + e^{i\vec{k}\vec{a}_2})\langle \phi_A |H|\phi_A\rangle = EA \qquad\qquad (D.1)$$

For site B, we have ($n_i=0$, $n_j=-1$), ($n_i=-1$, $n_j=0$), ($n_i=0$, $n_j=0$).

$$\left|\psi_k\right\rangle = B\left|\phi_B\right\rangle + A\left|\phi_A\right\rangle + Ae^{-i\vec{k}\vec{a}_1}\left|\phi_A\right\rangle + Ae^{i\vec{k}\vec{a}_2}\left|\phi_A\right\rangle$$

$$\left\langle\phi_B\mid\phi_B\right\rangle = 1, \left\langle\phi_B\mid\phi_A\right\rangle = 0$$

$$B\left\langle\phi_B\left|H\right|\phi_B\right\rangle + A(1 + e^{-i\vec{k}\vec{a}_1} + e^{-i\vec{k}\vec{a}_2})\left\langle\phi_A\left|H\right|\phi_A\right\rangle = EB \qquad\qquad (D.2)$$

Take equation D.1 and D.2 and solve for Eigenvalue E.

We set the onsite orbital energy term as α, $\left\langle\phi_A\left|H\right|\phi_A\right\rangle = \left\langle\phi_B\left|H\right|\phi_B\right\rangle = \alpha$.

Hopping energy term as β, $\left\langle\phi_A\left|H\right|\phi_B\right\rangle = \beta, \left\langle\phi_B\left|H\right|\phi_A\right\rangle = \beta^*$.

$$\gamma = 1 + e^{i\vec{k}\vec{a}_1} + e^{i\vec{k}\vec{a}_2}, \gamma^* = 1 + e^{-i\vec{k}\vec{a}_1} + e^{-i\vec{k}\vec{a}_2}$$

Combining the two equation, we can get

$$\begin{pmatrix} \alpha - E & \beta\gamma \\ \beta\gamma^* & \alpha - E \end{pmatrix}\begin{pmatrix} A \\ B \end{pmatrix} = E\begin{pmatrix} A \\ B \end{pmatrix}$$

$$\det\begin{pmatrix} \alpha - E & \beta\gamma \\ \beta\gamma^* & \alpha - E \end{pmatrix} = 0$$

$$(\alpha - E)^2 - |\beta|^2|\gamma|^2 = 0$$

$$E = \frac{2\alpha \pm \sqrt{(-2\alpha)^2 - 4\left[\alpha^2 - |\beta|^2|\gamma|^2\right]}}{2}$$

$$E = \alpha \pm |\beta||\gamma|$$

$$|\gamma||\gamma^*| = \left(1 + e^{i\vec{k}\vec{a}_1} + e^{i\vec{k}\vec{a}_2}\right)\left(1 + e^{-i\vec{k}\vec{a}_1} + e^{-i\vec{k}\vec{a}_2}\right)$$

$$|\gamma||\gamma^*| = 3 + 2\cos(\vec{k}\vec{a}_1) + 2\cos(\vec{k}\vec{a}_2) + 2\cos(\vec{k}(\vec{a}_1 - \vec{a}_2))$$

$$|\gamma| = \sqrt{3 + 2\cos(\vec{k}\vec{a}_1) + 2\cos(\vec{k}\vec{a}_2) + 2\cos(\vec{k}(\vec{a}_1 - \vec{a}_2))}$$

$$\vec{a}_1 = (\frac{a}{2}, \frac{\sqrt{3}a}{2}), \;\; \vec{a}_2 = (-\frac{a}{2}, \frac{\sqrt{3}a}{2})$$

$$|\gamma| = \sqrt{3 + 2\cos(k_x\frac{a}{2} + k_y\frac{\sqrt{3}a}{2}) + 2\cos(-k_x\frac{a}{2} + k_y\frac{\sqrt{3}a}{2}) + 2\cos(k_x a)}$$

$$|\gamma| = \sqrt{3 + 4\cos(k_x\frac{a}{2})\cos(k_y\frac{\sqrt{3}a}{2}) + 2\cos(k_x a)}$$

Therefore, we have

$$E(k_x, k_y) = \alpha \pm |\beta| \left\{ 1 + 4\cos\left(\frac{k_x a}{2}\right)\cos\left(\frac{\sqrt{3}k_x a}{2}\right) + 4\cos^2\left(\frac{k_x a}{2}\right) \right\}^{1/2}$$

Bibliography

[1]   G. Moore, Electronics **38** (1965).

[2]   M. N. Baibich *et al.*, Phys. Rev. Lett. **61**, 2472 (1988).

[3]   J. S. Moodera *et al.*, Phys. Rev. Lett. **74**, 3273 (1995).

[4]   S. S. P. Parkin *et al.*, Nature Materials **3**, 862 (2004).

[5]   S. Yuasa *et al.*, Nature Materials **3**, 868 (2004).

[6]   K. S. Novoselov *et al.*, Science **306**, 666 (2004).

[7]   K. S. Novoselov *et al.*, Proc. Natl. Acad. Sci. U.S.A. **102**, 10451 (2005).

[8]   Y. Zhang *et al.*, Nature **438**, 201 (2005).

[9]   A. K. Geim, and K. S. Novoselov, Nature Materials **6**, 183 (2007).

[10]   S. Adam, and S. Das Sarma, Solid State Comm. **146**, 356 (2008).

[11]   Y.-W. Tan *et al.*, Phys. Rev. Lett. **99**, 246803 (2007).

[12]   K. I. Bolotin *et al.*, Phys. Rev. Lett. **101**, 096802 (2008).

[13]   Y. Zhang *et al.*, Phys. Rev. Lett. **96**, 136806 (2006).

[14]   C. Todblacke *et al.*, Phys. Rev. B **74**, 235417 (2006).

[15]   K. I. Bolotin *et al.*, Nature **462**, 196 (2009).

[16]   X. Du *et al.*, Nature **462**, 192 (2009).

[17]   Y.-M. Lin *et al.*, Nano Lett. **9**, 422 (2008).

[18]   F. Schedin *et al.*, Nature Materials **6**, 652 (2007).

[19]   J. H. Chen *et al.*, Nature Physics **4**, 377 (2008).

[20]   D. B. Farmer *et al.*, arXiv:0812.1742 (2008).

[21]   S. Adam *et al.*, Solid State Comm. **149**, 1072 (2009).

[22]   E. H. Hwang, S. Adam, and S. Das Sarma, Phys. Rev. Lett. **98** (2007).

[23]   S. D. Sarma *et al.*, arXiv:1003.4731 (2010).

[24]   J.-H. Chen *et al.*, Nature Nanotech. **3**, 206 (2008).

[25]   E. H. Hwang, and S. Das Sarma, Phys. Rev. B **77**, 115449 (2008).

[26]   M. Ishigami *et al.*, Nano Lett. **7**, 1643 (2007).

[27]   F. J. Jedema, A. T. Filip, and B. J. van Wees, Nature **410**, 345 (2001).

[28]   F. J. Jedema *et al.*, Appl. Phys. Lett. **81**, 5162 (2002).

[29]   A. T. Hanbicki *et al.*, Appl. Phys. Lett. **82**, 4092 (2003).

[30]   X. Lou *et al.*, Nature Physics **3**, 197 (2007).

[31]   X. Lou *et al.*, Phys. Rev. Lett. **96**, 176603 (2006).

[32]   Z. H. Xiong *et al.*, Nature **427**, 821 (2004).

[33]   K. Tsukagoshi, B. W. Alphenaar, and H. Ago, Nature **401**, 572 (1999).

[34]   L. E. Hueso *et al.*, Nature **445**, 410 (2007).

[35]   N. Tombros *et al.*, Phys. Rev. Lett. **101**, 046601 (2008).

[36]   S. Cho, Y.-F. Chen, and M. S. Fuhrer, Appl. Phys. Lett. **91**, 123105 (2007).

[37]   E. W. Hill *et al.*, IEEE Trans. Magn. **42**, 2694 (2006).

[38]   W. H. Wang *et al.*, Phys. Rev. B (Rapid Comm.) **77**, 020402 (2008).

[39]   N. Tombros *et al.*, Nature, 571 (2007).

[40]   D. Huertas-Hernando, F. Guinea, and A. Brataas, Eur. Phys. J. Spec. Top. **148**, 1951 (2007).

[41]   D. Huertas-Hernando, F. Guinea, and A. Brataas, Phys. Rev. B **74**, 155426 (2006).

[42]   A. H. Castro Neto, and F. Guinea, Phys. Rev. Lett. **103**, 026804 (2009).

[43]   C. Ertler *et al.*, Phys. Rev. B (Rapid Comm.) (2009).

[44]   K. Pi *et al.*, Phys. Rev. Lett. **104**, 187201 (2010).

[45]   M. Popinciuc *et al.*, Phys. Rev. B **80**, 214427 (2009).

[46]   C. Józsa *et al.*, Phys. Rev. B (Rapid Comm.) **80**, 241403 (2009).

[47]   C. Berger *et al.*, Science **312**, 1191 (2006).

[48]   K. S. Kim *et al.*, Nature **457**, 706 (2009).

[49]   K. Pi *et al.*, Phys. Rev. B **80**, 075406 (2009).

[50]   G. Giovannetti *et al.*, Phys. Rev. Lett. **101**, 026803 (2008).

[51]   P. A. Khomyakov *et al.*, Phys. Rev. B **79**, 195425 (2009).

[52]   A. C. Ferrari *et al.*, Phys. Rev. Lett. **97**, 187401 (2006).

[53]   S. N. M. Bajuri *et al.*, 1st National Conference on Electronic Design, 81 (2005).

[54]   M. Ishigami *et al.*, Nano Lett. **7**, 1643 (2007).

[55]   S. Takahashi, and S. Maekawa, Phys. Rev. B **67**, 052409 (2003).

[56]   M. I. Katsnelson, F. Guinea, and A. K. Geim, Phys. Rev. B **79**, 195426 (2009).

[57]   B. Uchoa *et al.*, Phys. Rev. Lett. **101**, 026805 (2008).

[58]   B. Uchoa, C.-Y. Lin, and A. H. Casto Neto, Phys. Rev. B **77**, 035420 (2008).

[59]   A. V. Krasheninnikov *et al.*, Phys. Rev. Lett. **102** (2009).

[60]   B. Uchoa, and A. H. Castro Neto, Phys. Rev. Lett. **98**, 146801 (2007).

[61]   K. T. Chan, J. B. Neaton, and M. L. Cohen, Phys. Rev. B **77**, 235430 (2008).

[62]   Y. Mao, J. Yuan, and J. Zhong, J. Phys.: Condens Matter **20**, 115209 (2008).

[63]   G. Giovannetti *et al.*, Phys. Rev. Lett. **101**, 026803 (2008).

[64] E. J. H. Lee *et al.*, Nat. Nanotechnol. **3**, 486 (2008).

[65] F. Xia *et al.*, Nano Lett. **9**, 1039 (2009).

[66] B. Huard *et al.*, Phys. Rev. B (Rapid Comm.) **78**, 1214202 (2008).

[67] J. Park, Y. H. Ahn, and C. Ruiz-Vargas, Nano Lett. **9**, 1742 (2009).

[68] H. Sevincli *et al.*, Phys. Rev. B **77**, 195434 (2008).

[69] M. I. Rojas, and E. P. M. Leiva, Phys. Rev. B **76**, 155415 (2007).

[70] *CRC Handbook of Chemistry and Physics* (CRC Press, 2008).

[71] N. Ooi, A. Rairkar, and J. B. Adams, Carbon **44**, 231 (2006).

[72] S. J. Sque, R. Jones, and P. R. Briddon, Physica Status Solidi **204**, 3078 (2007).

[73] E. J. H. Lee *et al.*, Nature Nanotech. **3**, 486 (2008).

[74] S. V. Morozov *et al.*, Phys. Rev. Lett. **100**, 016602 (2008).

[75] P. R. Wallace, Physical Review **71**, 622 (1947).

[76] T. Stauber, N. M. R. Peres, and A. H. C. Neto, Phys. Rev. B (2008).

[77] K. M. McCreary *et al.*, Phys. Rev. B **81**, 115453 (2010).

[78] R. Ramprasad, P. von Allmen, and L. R. C. Fonseca, Phys. Rev. B **60**, 6023 (1999).

[79] P. A. Khomyakov *et al.*, Phys. Rev. B **79**, 195425 (2009).

[80] M. A. Pushkin *et al.*, Bulletin of the Russian Academy of Science: Physics **72**, 878 (2008).

[81] F. Schedin *et al.*, Nat. Mat. **6**, 652 (2007).

[82] N. Tombros, S. J. v. d. Molen, and B. J. van Wees, Phys. Rev. B **73**, 233403 (2006).

[83]   D. S. Novikov, Phys. Rev. B **76**, 245435 (2007).

[84]   S. A. Wolf *et al.*, Science **294**, 1488 (2001).

[85]   N. Tombros *et al.*, Nature **448**, 571 (2007).

[86]   W. Han *et al.*, Phys. Rev. Lett. **102**, 137205 (2009).

[87]   H. Min *et al.*, Phys. Rev. B **74**, 165310 (2006).

[88]   Y. Yao *et al.*, Phys. Rev. B **75**, 041401(R) (2007).

[89]   D. Huertas-Hernando, F. Guinea, and A. Brataas, Phys. Rev. Lett. **103**, 146801 (2009).

[90]   W. Han *et al.*, Appl. Phys. Lett. **94**, 222109 (2009).

[91]   C. Jozsa *et al.*, arXiv:0910.1054 (2009).

[92]   M. Shiraishi *et al.*, Adv. Func. Mater. **19**, 1 (2009).

[93]   D. Huertas-Hernando, F. Guinea, and A. Brataas, Eur. Phys. J. Special Topics **148**, 177 (2007).

[94]   C. Ertler *et al.*, Phys. Rev. B **80**, 041405(R) (2009).

[95]   T. Ando, J. Phys. Soc. Japan **75**, 074716 (2006).

[96]   C. Jang *et al.*, Phys. Rev. Lett. **101**, 146805 (2008).

[97]   F. Meier, and B. P. Zachachrenya, *Optical Orientation, Modern Problems in Condensed Matter Science* (North-Holland, Amsterdam, 1984), Vol. 8.

[98]   H. Hoevel, and I. Barke, Prog. Surf. Sci. **81**, 53 (2006).

[99]   I. Gierz *et al.*, Nano Lett. **8**, 4603 (2008).

[100]   S. Takahashi, and S. Maekawa, Phys. Rev. B **67**, 052409 (2003).

[101]   T. Kimura, Y. Otani, and J. Hamrle, Phys. Rev. B **73**, 132405 (2006).

[102]   Y. Gan, L. Sun, and F. Banhart, Small **4**, 587 (2008).

[103]   S. Molola, H. Hakkinen, and P. Koskinen, Appl. Phys. Lett. **94**, 043106 (2009).

[104]   Z. M. Ao *et al.*, J. Appl. Phys. **105**, 074307 (2009).

[105]   W. Han *et al.*, arXiv:1003.2669v2 (2010).

[106] R. Verucchi, and S. Nannarone, Review of Scientific Instruments **71**, 3444 (2000).